https://dx.doi.org/10.1016/j.combustflame.2023.113175

Theoretical study of H-atom abstraction by $CH_3O\dot{O}$ radicals from aldehydes and alcohols: *ab initio* and comprehensive kinetic modeling

Ruoyue Tang[a], Yu Han[a], Hao Chen[b], Bei Qu[b], Yang Li[c,*], Zhewen Lu[d], Ziheng Xing[e], Song Cheng[a,f,*]

[a] Department of Mechanical Engineering, The Hong Kong Polytechnic University, Kowloon 999077, Hong Kong

[b] Xi'an Modern Chemistry Research Institute, Northwestern Polytechnical University Xi'an, Shaanxi 710065, China

[c] Science and Technology on Combustion, Internal Flow and Thermostructure Laboratory, School of Astronautics, Northwestern Polytechnical University Xi'an, Shaanxi 710072, China

[d] Faculty of Maritime and Transportation, Ningbo University, Ningbo, Zhejiang 315211, China

[e] Group Sustainable Development Department, Cathay Pacific Airways Limited, Lantau 999077, Hong Kong

[f] Research Centre for Resources Engineering towards Carbon Neutrality, The Hong Kong Polytechnic University, Kowloon 999077, Hong Kong

* Correspondence: songryan.cheng@polyu.edu.hk, yang.li@nwpu.edu.cn.

Abstract

Reaction kinetics of H-atom abstraction from C_1-C_3 alcohols, including CH_3OH, C_2H_5OH, NC_3H_7OH, IC_3H_7OH, and C_1-C_2 aldehydes, including CH_2O, CH_3CHO, by $CH_3O\dot{O}$ radicals is investigated in this work through high-level *ab initio* calculations. Electronic structure optimizations are performed for all the stationary points with M06-2X/6−311++g(d,p) method. Quadratic configuration interaction method QCISD(T)/cc-pVXZ (where X = D and T) and Møller–Plesset perturbation theory MP2/cc-pVXZ (where X = D, T, and Q) are used to calculate single point energies. Subsequently, rate coefficients for all H-atom abstraction channels are determined using conventional transition state theory with unsymmetric tunneling corrections. These calculated results are updated to a recently updated model and then compared against expansive experimental datasets to investigate their influence on the model prediction performance. The updated model shows obvious discrepancies with the original model, where the updated model is less reactive for CH_3CHO, C_2H_5OH, NC_3H_7OH, and IC_3H_7OH, while showing negligible differences for CH_3OH and CH_2O due to the lack of $CH_3O\dot{O}$ radical formation. Sensitivity and flux analyses are further conducted, through which the difference between the studied species in their oxidation pathways and the relative importance of H-atom abstraction by $CH_3O\dot{O}$ radicals is highlighted. With the updated rate parameters, the branching ratios of H-atom abstractions from CH_2O and CH_3CHO are significantly altered for CH_3CHO, C_2H_5OH, NC_3H_7OH and IC_3H_7OH, with an obvious shift away from the abstraction channel by $CH_3O\dot{O}$. Further analyses highlight the critical roles of CH_2O and CH_3CHO chemistry as core chemistries for large hydrocarbons (e.g., carbon number >1), which have been inadequately described in existing chemistry models. Systematic efforts are urgently needed to improve the existing CH_2O and CH_3CHO chemistries.

Keywords: H-atom abstraction reaction; methyl peroxy radical; high-level *ab initio* calculations; C_1-C_3 alcohols; C_1-C_2 aldehyde.

Novelty and Significance Statement

- The rate parameters of H-atom abstraction from CH_2O, CH_3CHO, CH_3OH, C_2H_5OH, NC_3H_7OH, and IC_3H_7OH by $CH_3O\dot{O}$ radicals are determined through high-level *ab initio* calculations for the first time, and thereafter systematically compared with their similarities and differences highlighted.
- Comprehensive model implementation is carried out, where the calculated reactions exhibit considerable impact on model performance, with overall better agreements observed with experiments.
- This study reveals the considerably different oxidation pathways for C1 species and their heavier counterparts, where $CH_3O\dot{O}$-related kinetics play completely different roles.
- This study also reveals the critical roles of CH_2O and CH_3CHO sub-chemistries, which have been ill-conditioned in existing models, in developing adequate chemistry models for large hydrocarbons (e.g., carbon number >1), and call for future efforts to improve the current CH_2O and CH_3CHO chemistries.

Authors Contributions statement

Ruoyue Tang: Data analysis, Original draft preparation, Validation. **Yu Han:** Data analysis, Investigation. **Hao Chen:** Investigation. **Qu Bei:** Investigation. **Yang Li:** Designed research, Methodology. **Zhewen Lu:** Data curation. **Ziheng Xing:** Data curation. **Song Cheng:** Designed research, Methodology, Conceptualization, Review & editing, Funding acquisition, Project management.

1. Introduction

Short carbon chain alcohols, e.g., methanol (CH_3OH), ethanol (C_2H_5OH), and propanol (C_3H_7OH), have been the most promising candidates for petroleum-derived gasoline additives, due to their ability to improve engine efficiency [1] and reduce emissions, in particular NOx [2], carbon monoxide (CO), and particulate matter (PM) [3]. Derived from biological sources, the renewability of alcohols makes them more competitive [4]. Many researchers have studied the impacts of alcohols on the emissions and combustion characteristics of SI engines [5, 6] and CI engines [7, 8, 9].

As one of the most abundant toxic oxygenated emissions, aldehydes are released into the atmosphere after partial combustion of traditional fuel and biofuel, causing damage to the environment and human health [10]. Besides, they are recognized as important intermediates formed during the combustion of hydrocarbon [11]. For instance, formaldehyde (CH_2O) concentration is high during methanol oxidation [12]. Acetaldehyde (CH_3CHO) can be formed after the dehydrogenation of ethanol [13]. Therefore, further understanding of aldehydes combustion mechanism is crucial to developing kinetic models for practical fuels, especially biofuel.

Developing chemical kinetic models for the blends of biofuels and petroleum-derived fuels helps get accurate predictions of combustion behavior and accelerate practical implementation. Generally, a multi-component chemical kinetic model can be obtained by simply combining chemical kinetic models of each single fuel, sometimes, with some modifications to the important reactions. Nonetheless, due to the neglect of interactions between each component, these combined models always show inadequacies in predicting the combustion behavior of blends. For instance, a state-to-the-art chemical kinetic model for biofuels and petroleum-derived fuels blends proposed by Cheng and co-workers can capture the experimental results of neat alcohols and neat gasoline well, while showing increasing disagreement with the experimental results of gasoline surrogate and ethanol blends at higher levels of ethanol blending [14]. Later, they attributed these drawbacks to the lack of interaction between alcohols and gasoline sub-chemistries, emphasizing the necessity of further investigation for interaction between methylperoxy radical ($CH_3O\dot{O}$) and alcohols [8].

$CH_3O\dot{O}$, a member of alkyl peroxy ($RO\dot{O}$), is a crucial radical in low to intermediate temperature chemistry, which always forms via $CH_3+O_2 = CH_3O\dot{O}$ and participates in the chain reactions to sustain autoignition in low temperatures [15]. Besides, it is believed to be crucial in H-atom abstraction reactions, i.e., $CH_3O\dot{O}+RH = CH_3OOH+R$. Curran [16] highlighted that $CH_3O\dot{O}$ radical is an important abstractor at intermediate temperatures, especially for species that can produce high concentration of CH_3. Kuzhanthaivelan and Rajakumar [17] reported that H-atom abstraction reactions of

dimethoxymethane by peroxy radicals (namely HO_2 and $CH_3O\dot{O}$) affect the ignition of dimethoxymethane.

With the increasing attention drawn to H-atom abstraction reactions by $CH_3O\dot{O}$ radical, researchers have tried to characterize them by high-level quantum chemical calculation. Carstensen et al. [18] calculated the rate coefficients for H-atom abstraction from several alkanes by $CH_3O\dot{O}$, i.e., CH_4, C_2H_6, C_3H_8, C_4H_{10}, at the CBS-QB3//B3LYP/CBSB7 level of theory. Guo et al. [19] investigated the detailed kinetic properties of dehydrogenation by $CH_3O\dot{O}$ from species up to C_7, including alkanes, alkenes, dienes, alkynes, ethers, and ketones. The H-atom abstractions from different sites of different species are studied and compared. Shi et al. [20] determined the rate coefficient of $CH_3O\dot{O}+ CH_2O = CH_3OOH+HCO$ over the temperature range of 300 - 1500 K based on transition state theory. Zhang et al. [21] proposed the rate coefficients of $CH_3O\dot{O}+CH_3CHO = CH_3OOH+CH_2CHO$ and $CH_3O\dot{O}+CH_3CHO = CH_3OOH+CH_3CO$ at 300 - 1500 K, which are represented in double-Arrhenius expression. Song and co-workers [22, 23] determined the rate coefficient for H-atom abstraction from CH_3OH and C_2H_5OH by $CH_3O\dot{O}$ radical using *ab initio* calculations, noting that $CH3O\dot{O}+CH_3OH = CH_3OOH+CH_2OH$ and $CH_3O\dot{O}+C_2H_5OH = CH_3OOH+CH_3CHOH$ being the dominating channels.

To develop a chemical kinetic model of gasoline surrogate/bio-fuel blend with better performance, Yang et al. [24] conducted the high-level theoretical kinetic calculations of H-atom abstraction from gasoline surrogate components by $CH_3O\dot{O}$, including cyclopentane, toluene, 1-hexene, n-heptane, and isooctane. To further this effort, a detailed theoretical study of H-atom abstractions by $CH_3O\dot{O}$ from biofuels, e.g., CH_3OH, C_2H_5OH, NC_3H_7OH, and IC_3H_7OH, and species that are frequently produced during oxidation of alcohols, e.g., CH_2O and CH_3CHO, is performed in this study. The energy barriers and rate coefficients of individual reactions are provided. The influence of these calculated reactions is investigated by updating them to a previous model [14]. Sensitivity analysis and flux analysis for each fuel are carried out to illustrate the reasons for the changes caused by these reactions.

2. Computational methods

In this study, a series of *ab initio* computations have been performed using the same methods adopted by recent studies [19, 24]. Specifically, the M06-2X functional [25] with the 6-311++G(d,p) basis set [26,27] is used for geometry optimizations, vibrational frequencies calculations, zero-point energy (ZPE) calculations, dihedral angle scans for conformer search and the low-frequency modes. Internal rotations are scanned as a function of dihedral angle with 10-degree increments for optimized reactants, products and transition states to ensure that the obtained structure has the

minimum energy. The rigid-rotor-harmonic-oscillator (RRHO) model is employed to characterize the rotational-vibrational degrees of freedom, while the 1-D hindered rotor approximation is applied for the low-frequency torsional modes. Intrinsic reaction coordinate (IRC) calculation is performed for each transition state to confirm the transition state connects the desired reactants and products. According to the recommendations for the M06-2X method by Zhao and Truhlar [25], the harmonic frequencies and ZPEs scale factors are 0.983 and 0.9698, respectively. The optimized structures of the reactants, radicals, transition states and complexes are provided in the Supplementary Material. To refine the electronic energy, single point energies (SPEs) for all species were performed at the quadratic configuration interaction method QCISD(T)/cc-pVXZ (where X = D and T) [28] and Møller–Plesset perturbation theory MP2/cc-pVXZ (where X = D, T and Q) [29]. The SPEs are extrapolated to the complete basis set (CBS) limit using the following equation [30]:

E_{CBS} = QCISD(T)/TZ+[QCISD(T)/TZ-QCISD(T)/DZ]×0.4629+MP2/QZ+[MP2/QZ-MP2/TZ]×0.6938-{MP2/TZ+[MP2/TZ-MP2/DZ]×0.4629}

The MultiWell [31] program suite is used to determine the high-pressure limiting rate constants based on the canonical transition state theory. The Lamm module is used to calculate external rotational constants and reduced moments of inertia for the hindered internal rotations [32]. The calculated results are then fitted to truncated Fourier series, which are further used as 1-D hindered internal rotation input in the Thermo module. The Master Equation System Solver (MESS) program suite [33] is employed here to calculate the chemical rate coefficients for complex-forming reactions via solution of the one-dimensional master equation, based on the chemically significant eigenstate approach of Miller and Klippenstein [34] and the bimolecular species model of Georgievskii and Klippenstein [35]. In both program suites, quantum mechanical tunneling corrections assuming the asymmetric Eckart potential (TST/Eck) [36] are applied to obtain the rate coefficient over the temperature range of 298–2000 K. All rate coefficients were fitted to the modified Arrhenius equation, which can be defined as $k = AT^nEXP(-E_a/RT)$. The fitted rate parameters are summarized in the Supplementary Material.

3. Results and discussion

3.1 Species and reaction sites

This study involves two aldehydes and four alcohols, with a total of 11 reactions. To better illustrate these reactions, the different sites of each species are marked, as shown in Fig 1. According to the type of C-atoms to which H-atoms bond, the H-atoms are divided into primary hydrogen (labeled P), secondary hydrogen (labeled S), and tertiary hydrogen (labeled T). According to the proximity to the functional group, H-atoms are

labeled again as α, β, and γ. Specially, the H-atom in aldehyde group is labeled as ν.

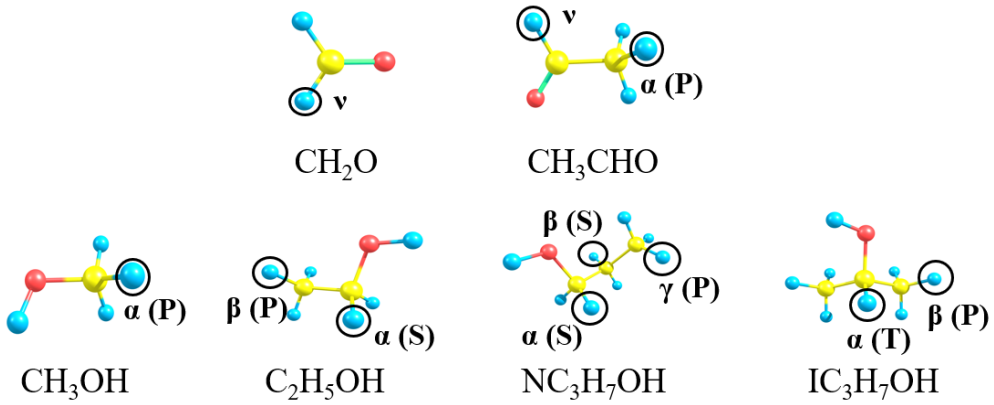

Fig. 1. Different abstraction sites in CH_2O, CH_3CHO, CH_3OH, C_2H_5OH, NC_3H_7OH, and IC_3H_7OH.

3.2 Electronic Energy Barriers

The forward and reverse reaction energy barriers for H-atom abstraction by $CH_3O\dot{O}$ radical from different sites of CH_2O, CH_3CHO, CH_3OH, C_2H_5OH, NC_3H_7OH, and IC_3H_7OH are summarized in Table 1. It is found that for the forward reactions, the energy barriers for the abstraction of primary hydrogens are the highest. For instance, the energy barrier for H-atom abstraction from C_2H_5OH is 22.42 kcal/mol for primary hydrogen and decreases to 13.76 kcal/mol for secondary hydrogen. The reaction of primary hydrogen abstraction from C_2H_5OH has the highest energy barrier among all reactions, with a value of 22.42 kcal/mol. There are two kinds of secondary hydrogen in NC_3H_7OH which are recognized as α hydrogen and β hydrogen, with energy barrier of β hydrogen abstraction (16.13 kcal/mol) being higher than that of α hydrogen (13.61 kcal/mol).

For aldehydes, the energy barrier for H-atom abstraction from ν site of CH_2O (13.00 kcal/mol) is slightly higher than that of CH_3CHO (11.52 kcal/mol), indicating that aldehydic hydrogen abstraction from CH_3CHO is easier than from CH_2O. For alcohols, the highest energy barrier for α hydrogen abstraction is 16.13 kcal/mol for CH_3OH, which decreases to 13.76 kcal/mol for C_2H_5OH and 13.61 kcal/mol for NC_3H_7OH and 11.76 kcal/mol for IC_3H_7OH.

Table 1. The energy barriers (in kcal/mol) for H-atom abstraction by $CH_3O\dot{O}$ radical from different sites of aldehydes and alcohols.

No.	Reaction	Forward	Reverse
R1	$CH_2O + CH_3O\dot{O} = HCO + CH_3OOH$	13.00	10.86
R2	$CH_3CHO + CH_3O\dot{O} = CH_3CO + CH_3OOH$	11.52	8.41

R3	$CH_3CHO+CH_3O\dot{O}=CH_2CHO+CH_3OOH$	20.15	9.95
R4	$CH_3OH+CH_3O\dot{O}=CH_2OH+CH_3OOH$	16.13	5.8
R5	$C_2H_5OH+CH_3O\dot{O}=C_2H_4OH\_S+CH_3OOH$	13.76	4.77
R6	$C_2H_5OH+CH_3O\dot{O}=C_2H_4OH\_P+CH_3OOH$	22.42	6.14
R7	$NC_3H_7OH+CH_3O\dot{O}=NC_3H_6OH\_\alpha(S)+CH_3OOH$	13.61	4.19
R8	$NC_3H_7OH+CH_3O\dot{O}=NC_3H_6OH\_\beta(S)+CH_3OOH$	16.13	2.98
R9	$NC_3H_7OH+CH_3O\dot{O}=NC_3H_6OH\_P+CH_3OOH$	21.10	5.99
R10	$IC_3H_7OH+CH_3O\dot{O}=IC_3H_6OH\_T+CH_3OOH$	11.76	3.45
R11	$IC_3H_7OH+CH_3O\dot{O}=IC_3H_6OH\_P+CH_3OOH$	19.21	2.88

3.3 Rate coefficient results

3.3.1 Rate coefficient of different sites at the same species

The rate coefficients for H-atom abstraction by $CH_3O\dot{O}$ radical from different sites of CH_2O, CH_3CHO, CH_3OH, C_2H_5OH, NC_3H_7OH, and IC_3H_7OH are summarized in Table 2, given in an Arrhenius expression of $k = AT^nEXP(-E_a/RT)$.

Table 2. The rate coefficient for H-atom abstraction by $CH_3O\dot{O}$ radical from different aldehydes and alcohols

No.	Reaction	A (cm^3/ mole·s)	n	Ea (cal/ mole)
R1	$CH_2O+CH_3O\dot{O}=HCO+CH_3OOH$	8.24E+07	1.63	14207
		5.36E+04	1.65	7129
R2	$CH_3CHO+CH_3O\dot{O}= CH_3CO+CH_3OOH$	3.17E-06	5.20	5659
R3	$CH_3CHO+CH_3O\dot{O}= CH_2CHO+CH_3OOH$	4.45E-11	6.82	13466
R4	$CH_3OH+CH_3O\dot{O}=CH_2OH+CH_3OOH$	2.61E+04	2.47	19486
		1.17E+01	2.51	10816
R5	$C_2H_5OH+CH_3O\dot{O}=C_2H_4OH\_S+CH_3OOH$	5.23E+05	1.77	17382
		1.00E-02	3.24	8183
R6	$C_2H_5OH+CH_3O\dot{O}=C_2H_4OH\_P+CH_3OOH$	1.29E+22	-2.57	32110
		8.16E+11	-0.58	20089
R7	$NC_3H_7OH+CH_3O\dot{O}=NC_3H_6OH\_\alpha(S)+CH_3OOH$	9.19E-08	5.31	8936
R8	$NC_3H_7OH+CH_3O\dot{O}=NC_3H_6OH\_\beta(S)+CH_3OOH$	7.94E-05	4.50	12707
R9	$NC_3H_7OH+CH_3O\dot{O}=NC_3H_6OH\_P+CH_3OOH$	1.96E-04	4.96	17609
R10	$IC_3H_7OH+CH_3O\dot{O}=IC_3H_6OH\_T+CH_3OOH$	1.98E-07	5.55	4192

R11	$IC_3H_7OH+CH_3O\dot{O}=IC_3H_6OH\_P+CH_3OOH$	6.12E-07	5.62	8773

Figure 2 shows the rate coefficients in the temperature range of 298.15−2000 K for H-atom abstraction by $CH_3O\dot{O}$ radical at different sites of CH_2O and CH_3CHO. In the case of CH_3CHO (Fig. 3b), the rate coefficient for H-atom abstraction from ν site is about 10^7 higher than that from α site at 298.15 K. The prominent discrepancy between these two rate coefficients in the low-temperature range is consistent with the energy barrier shown in Table 1. Specifically, the energy barrier for H-atom abstraction from ν site is much lower than that from α site. This difference in rate coefficients of α site and ν site decreases rapidly with increasing temperature, with only about an eight-fold difference at a high temperature of 2000 K.

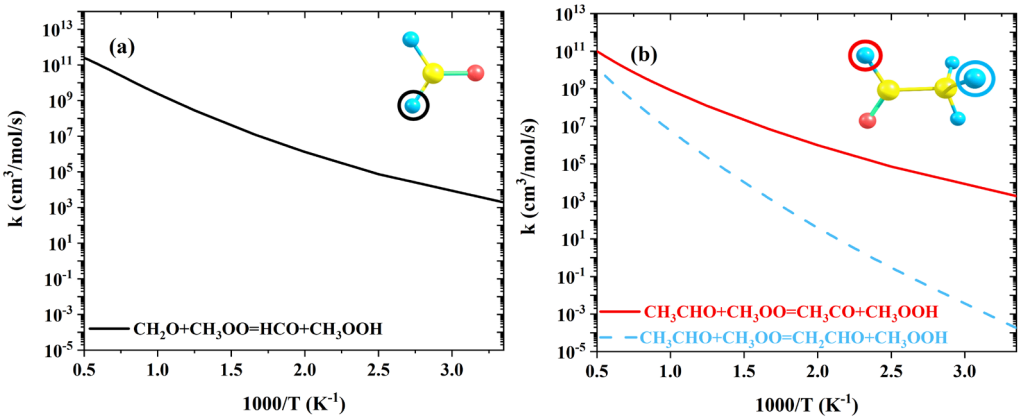

Fig. 2. The rate coefficients for H-atom abstraction by $CH_3O\dot{O}$ radical at different sites on (a) CH_2O and (b) CH_3CHO, on a per hydrogen atom basis.

The rate coefficients for H-atom abstraction by $CH_3O\dot{O}$ radical at different sites of alcohols, i.e., CH_3OH, C_2H_5OH, NC_3H_7OH, and IC_3H_7OH, are shown in Fig. 3. In the case of C_2H_5OH (Fig. 3b), the rate coefficient for H-atom abstraction from α site is about 4 orders of magnitude higher than that from β site at low temperature range. However, this difference decreases as temperature increases. After 1000 K, the former one is lower than the latter one. In the case of NC_3H_7OH (Fig. 3c), H-atom abstraction from α site is the fastest at low temperatures, while it is the lowest at higher temperatures. On the contrary, H-atom abstraction from γ site is the lowest at low temperatures, then increases to be the fastest at higher temperatures. The trend at low temperatures agrees with the energy barriers, where H-atom abstraction at α site is the lowest and that at γ site is the highest at low temperatures. The rate coefficient of γ hydrogen abstraction becomes higher than that of α hydrogen abstraction at higher temperatures due to the enhanced contribution of molecular vibration to system entropy. As for IC_3H_7OH (Fig. 3d), it is quite similar to the situation of C_2H_5OH, with H-atom abstraction from α site being faster than that from β site. The discrepancy between these

two rate coefficients decreases from several orders of magnitude at low temperatures to only approximately 6 times after 1900 K.

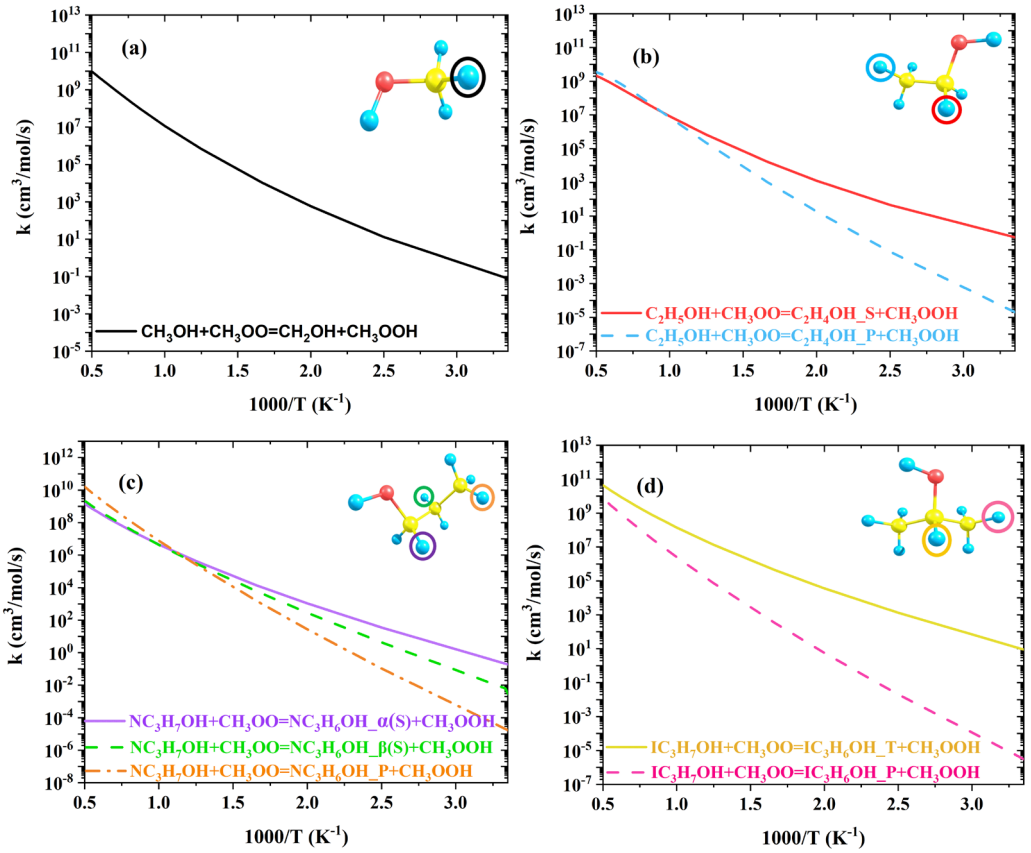

Fig. 3. The rate coefficients for H-atom abstraction by $CH_3O\dot{O}$ radical at different sites on (a) CH_3OH, (b) C_2H_5OH, (c) NC_3H_7OH, and (d) IC_3H_7OH, on a per hydrogen atom basis.

The rate coefficients for H-atom abstraction by $CH_3O\dot{O}$ radical from CH_2O calculated in this study are compared with the literature values [14, 20, 32], as shown in Fig. 4. These rate coefficients are in reasonable agreement with each other, with discrepancies between them being in 1 order of magnitude. The rate coefficient estimated by Tsang and Hampson [37] was obtained by analogy with a similar reaction $CH_2O+HO_2 = HCO+H_2O_2$ [37], with an uncertainty factor of 10. The rate coefficient proposed by Shi et al. [20] was calculated at M06-2X/6-311++G(d,p) level of theory. Both these two rate coefficients are close to the value calculated by this study and only show slight differences at low to intermediate temperature range. Cheng et al. [14] proposed the rate coefficient of $CH_2O+CH_3O\dot{O} = HCO+CH_3OOH$ by dividing the preexponential factor of $CH_2O+HO_2 = HCO+H_2O_2$ by 2. The discrepancy between this rate coefficient and the one calculated by this study becomes smaller as the temperature increases.

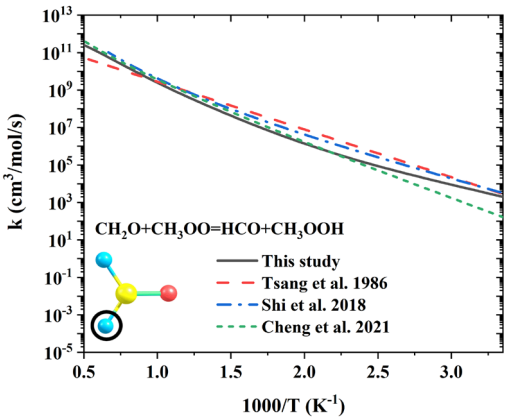

Fig. 4. The comparison between the rate coefficients for H-atom abstraction by $CH_3O\dot{O}$ radical from CH_2O calculated by this study and those from literature [14, 20, 37].

Figure 5 compares the rate coefficients for H-atom abstraction by $CH_3O\dot{O}$ radical from CH_3CHO calculated by this study with values from literature [21, 38]. For ν site, Fischer et al. [38] proposed the rate coefficient of $CH_3CHO+CH_3O\dot{O}$ = CH_3CO+CH_3OOH by analogy with CH_3CHO+R = CH_3CO+RH, which shows the largest discrepancy with the calculated rate coefficient of this study during intermediate temperatures of 600-800 K. The rate coefficient calculated by Zhang et al. [21] with CCSD(T)/cc-pVTZ//B2PLYPD3/cc-pVTZ method is in good agreement with the calculated value of this study. For α site, the rate coefficient calculated by this study and the value proposed by Zhang et al. [21] are almost coincident at higher temperature range and show a difference of less than one order of magnitude at lower temperatures.

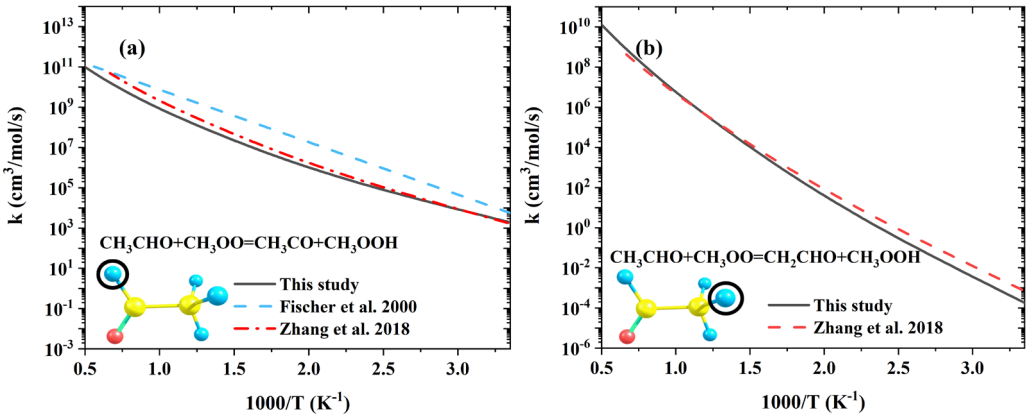

Fig. 5. The comparison between the rate coefficients for H-atom abstraction by $CH_3O\dot{O}$ radical from CH_3CHO calculated by this study and those from literature [21, 38].

Figure 6 shows the comparison between the rate coefficients for H-atom abstraction

by $CH_3O\dot{O}$ radical from CH_3OH calculated by this study and those from literature [22, 34]. Tsang [39] estimated the rate coefficient of $CH_3OH+CH_3O\dot{O} = CH_2OH+CH_3OOH$ based on the experimental measured rate coefficient at 600 K for reaction $CH_3O_2+CH_3OH+O_2 = CH_3O_2H+HO_2+CH_2O$ [40], with the uncertainty factor of 1.3 and 2.0 at 600 K and 1000 K, respectively. This rate is much higher than the one calculated from this study at low to intermediate temperatures. The calculated rate coefficient from Zhao et al. [22] is two orders of magnitude higher than that of this study at low temperatures. They optimized the geometries at MP2/aug-cc-pVTZ and performed SPE calculations at QCISD(T)/cc-pVTZ and CCSD(T)/aug-cc-pVTZ, which is different from the methods adopted by this study. The difference between the adopted theory seems to lead to the difference between these two calculated rate coefficients. As shown in Fig. S7 in the Supplementary Material, the energy surface calculated by Zhao et al. [22] shows an obvious difference from that of this study. On the other hand, although the rate coefficient proposed by Zhao et al. is in good agreement with the experiment [40], it should be noted that the experimental rate coefficient is measured for $CH_3O_2+CH_3OH+O_2 = CH_3O_2H +HO_2+CH_2O$ rather than the reaction calculated in this study.

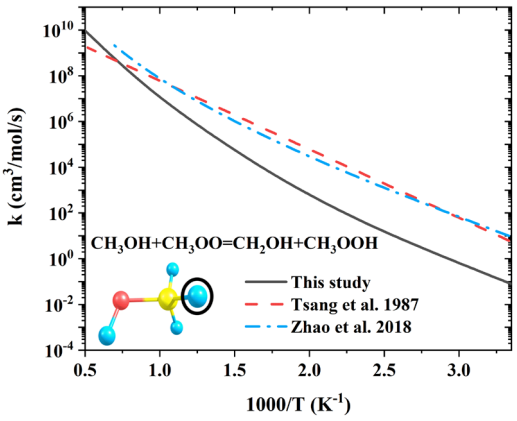

Fig. 6. The comparison between the rate coefficients for H-atom abstraction by $CH_3O\dot{O}$ radical from CH_3OH calculated by this study and those from literature [22, 39].

The rate coefficients for H-atom abstraction by $CH_3O\dot{O}$ radical from C_2H_5OH calculated by this study and those from literature [23, 41, 42] are compared in Fig. 7. For α site, the rate coefficient from Mittal et al. [41] is obtained by dividing the preexponential factor of $C_2H_5OH+HO_2 = C_2H_4OH\_S+H_2O_2$ [41] by 2. The rate coefficients from the kinetic model of Mehl et al. [42] and from Mittal et al. [41] are in good agreement with each other, while both being 1-2 orders of magnitude higher than the present results. The rate coefficient calculated by Shi et al. [23] is much higher than

that in this study, particularly at low temperatures. This is likely due to the different theories used and complex structures identified. Shi et al. [23] optimized the geometries at MP2/aug-cc-pVTZ and performed SPE calculations at QCISD(T)/cc-pVTZ and CCSD(T)/aug-cc-pVTZ, which is different from the one adopted by this study, as discussed in Section 2. The potential energy surfaces obtained from this study and Shi et al [23] are summarized in Fig. S8 in the Supplementary Material, where large discrepancies in energy are observed for the reactant complex and transition state. Similar trends are seen at the β site (Fig. 7b), which is, again, due primarily to the different energies of the reactant complex and transition state between this study and Shi et al [23], as shown in Fig. S9.

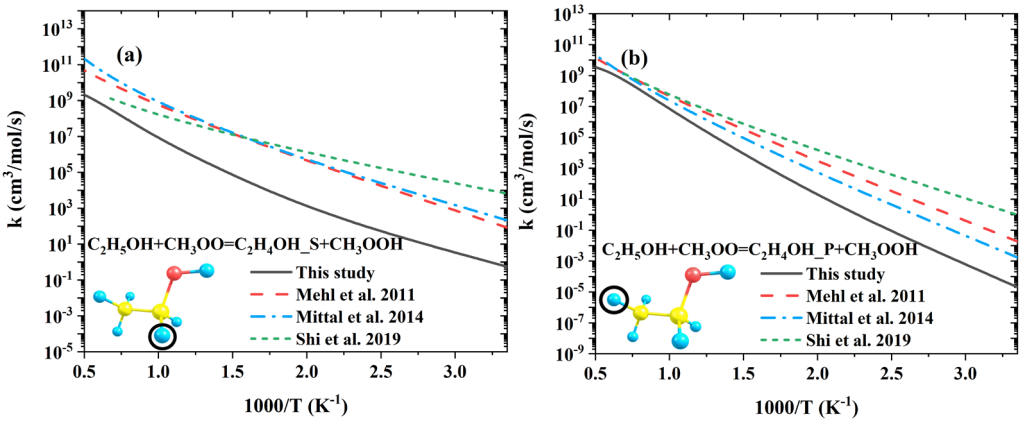

Fig. 7. The comparison between the rate coefficients for H-atom abstraction by $CH_3O\dot{O}$ radical from C_2H_5OH calculated by this study and those from literature [23, 41, 42].

Figure 8 shows the comparison between the rate coefficients for H-atom abstraction by $CH_3O\dot{O}$ radical from NC_3H_7OH calculated by this study and from Johnson et al. [43]. The rate coefficients for H-atom abstraction from α site and γ site proposed by Johnson et al. [43] are obtained by estimating them to be the same as the rate coefficients for H-atom abstraction by HO_2 from NC_3H_7OH at each corresponding point. It is found that for all the sites (α site, β site, and γ site), the rate coefficient calculated by this study is significantly lower than the values proposed by Johnson et al. [43].

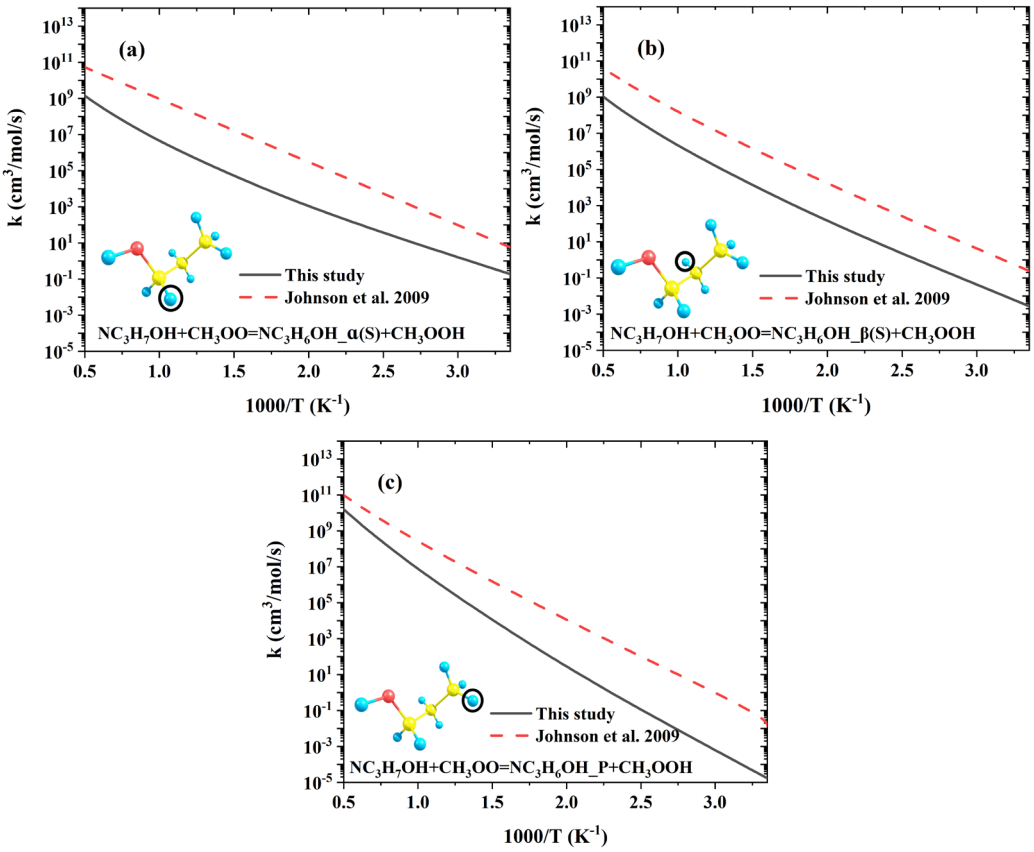

Fig. 8. The comparison between the rate coefficients for H-atom abstraction by $CH_3O\dot{O}$ radical from NC_3H_7OH calculated by this study and those from literature [43].

The comparisons between the rate coefficient for H-atom abstraction by $CH_3O\dot{O}$ radical from IC_3H_7OH calculated by this study and from Johnson et al. [43] are shown in Fig. 9. Same as the case of NC_3H_7OH, the rate coefficients for $IC_3H_7OH+CH_3O\dot{O}$ = $IC_3H_6OH+CH_3OOH$ are estimated to be the same as the values of $IC_3H_7OH+HO_2$ = $IC_3H_6OH+H_2O_2$. The rate coefficients of both sites proposed by Johnson et al. [43] are higher than that of this study. Compared with the situation of β site, the discrepancy between the value of this study and the value from Johnson et al. [43] is smaller for H-atom abstraction at α site.

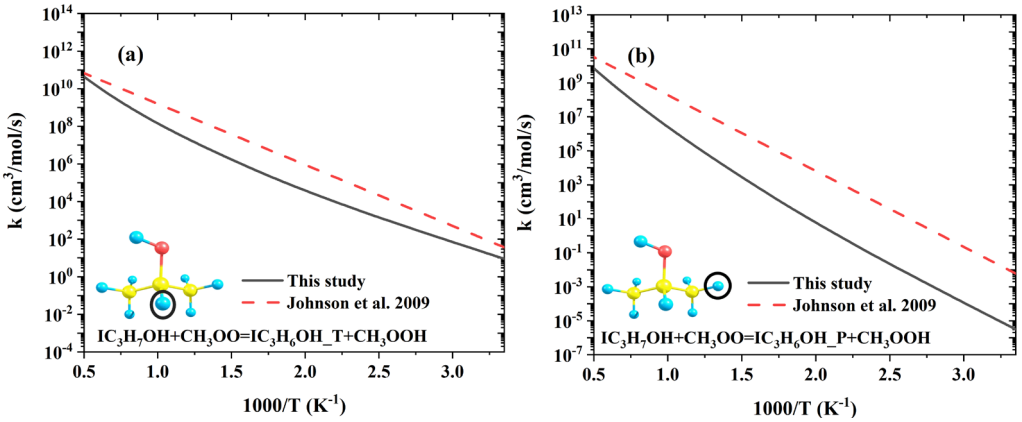

Fig. 9. The comparison between the rate coefficients for H-atom abstraction by $CH_3O\dot{O}$ radical from IC_3H_7OH calculated by this study and those from literature [43].

3.3.2 Comparison of rate coefficient between different species at the same site

H sites of aldehydes and alcohols are classified into α site, β site, and γ site according to its distance from the functional group and are classified into primary site, secondary site, and tertiary site according to the C-atom type. In this section, comparison of the same site between different species are shown.

Figure 10 shows the comparison at the primary site of CH_3CHO, CH_3OH, C_2H_5OH, NC_3H_7OH, and IC_3H_7OH. It can be seen that for most investigated species, i.e., CH_3CHO, C_2H_5OH, NC_3H_7OH, and IC_3H_7OH, their rate coefficients for H-atom abstraction from primary site are quite similar, especially at the high temperature range. In particular, the rate coefficients of C_2H_5OH and NC_3H_7OH are almost identical across the whole temperature range. The rate coefficient of CH_3OH is the highest at low temperatures, indicating that the H-atom abstraction from primary site of CH_3OH is the fastest, consistent with its lowest primary site energy barrier shown in Section 3.2.

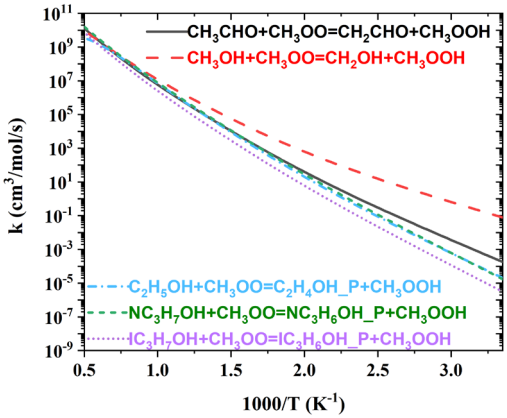

Fig. 10. Comparison of rate coefficients for H-atom abstraction at primary site of CH_3CHO, CH_3OH, C_2H_5OH, NC_3H_7OH, and IC_3H_7OH, on a per H atom basis.

Figure 11 shows the comparison between rate constants for abstraction at ν site of CH_2O and CH_3CHO. These two rate coefficients are very similar and only show a maximum difference of 3 times at high temperatures. This is consistent with the small deviation in the energy barrier between these two reactions, which is only 1.48 kcal/mol.

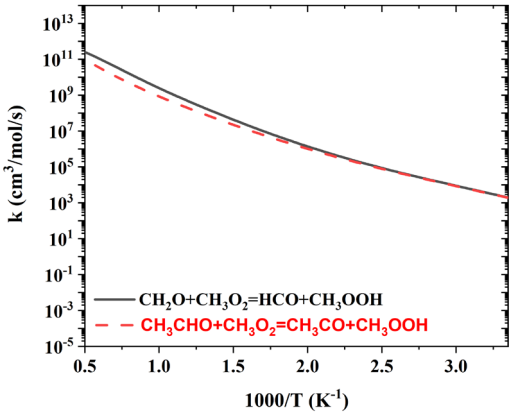

Fig. 11. Comparison of rate coefficients for H-atom abstraction at ν site of CH_2O and CH_3CHO, on a per H-atom basis.

Figure 12 shows the comparison of rate coefficients for abstraction at α site of CH_3CHO, CH_3OH, C_2H_5OH, NC_3H_7OH, and IC_3H_7OH. The rate coefficient of α hydrogen abstraction from CH_3CHO is the lowest at low temperatures, while it increases to a similar value to that from CH_3OH and C_2H_5OH at high temperatures. The difference between rate coefficients for α hydrogen abstraction from CH_3OH, C_2H_5OH, and NC_3H_7OH are within 1 order of magnitude. The H-atom abstraction from α site of IC_3H_7OH has the highest rate coefficient, which is related to its lowest energy barrier of 11.76 kcal/mol.

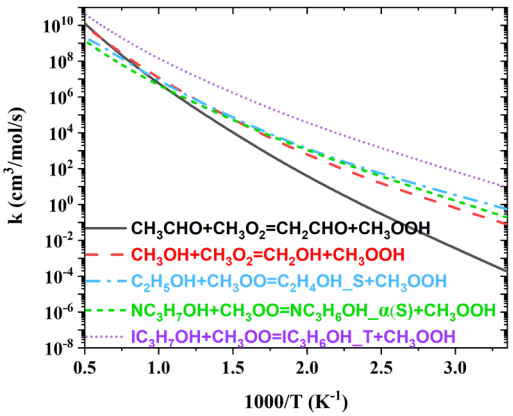

Fig. 12. Comparison of rate coefficients for H-atom abstraction at α site of CH_3CHO, CH_3OH, C_2H_5OH, NC_3H_7OH, and IC_3H_7OH, on a per H atom basis.

3.4 Model implementations

The chemistry model developed by Cheng et al. [14] is used herein to investigate the influence caused by these calculated reactions on the model performance in predicting combustion characteristics of CH_2O, CH_3CHO, CH_3OH, C_2H_5OH, NC_3H_7OH, and IC_3H_7OH. The development of the chemistry model has been documented in [14], hence will not be presented here. Particularly, the sub-chemistries of alcohols in the selected model have been improved recently, as summarized in [44,45]. The model without and with the updated rate parameters is referred to as "original model" and "updated model" in the following. It should be noted that the purpose of model implementations is to illustrate the impact of the reevaluated reactions, rather than to fix the model.

Simulations of the rapid compression machine (RCM) ignition delay times (IDTs) are completed using the LLNL-developed fast solver Zero-RK [46], including volume histories in non-reactive tests accounting for compression and heat loss [9]. The Plug Flow Reactor (PFR) and Perfectly Stirred Reactor (PSR) modules in Chemkin are used to conduct simulation of flow reactor and jet-stirred reactor (JSR). Reactions calculated in this study involve CH_3OO radical, which is a peroxyl radical that primarily forms in the low temperature range. Therefore, experimental results obtained at low temperatures are employed herein for model comparison. The most representative results are presented in the paper and the rest are provided in the Supplementary Materials.

Figure 13 compares the experimentally measured CH_2O and CO mole fraction profiles with the simulation results by original model and updated model. The experimental results are taken from [47] for CH_2O oxidation in a variable pressure flow reactor at initial temperatures of 850–950 K and at constant pressures ranging from 1.5 to 6.0 atm. It can be seen that the simulation results by updated model are almost identical with the simulation results by original model at different temperatures and pressures, where the experimental results show a more rapid oxidation rate than the simulation results.

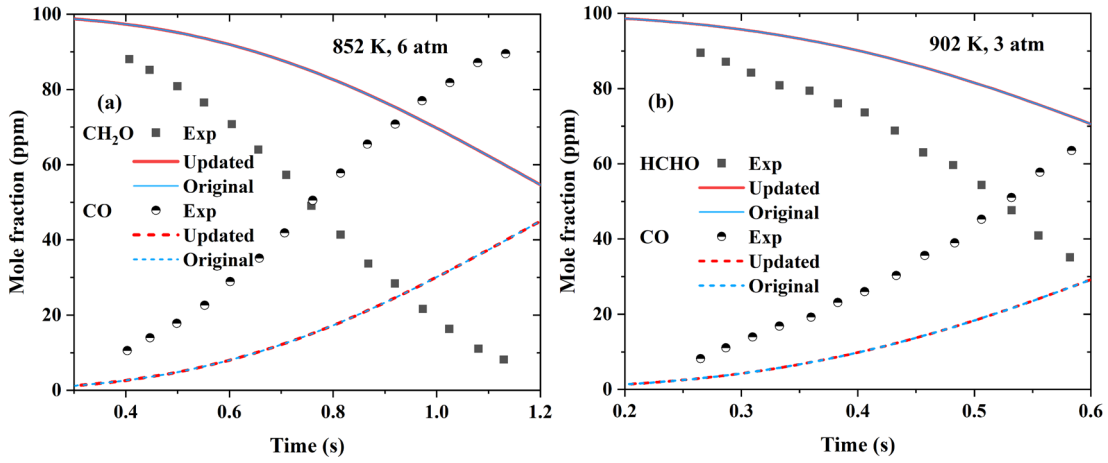

Fig. 13. Mole fraction profiles of CH_2O /H_2O/O_2/N_2 mixtures in a flow reactor. Symbols: experimental results [47]; Blue lines: simulation results by original model; Red lines: simulation results by updated model. Initial conditions are (a) CH_2O 100 ppm, O_2 1.5%, H_2O 0.35% with balance N_2 at 852 K and 6.0 atm; (b) CH_2O 100 ppm, O_2 2.0%, H_2O 0.34% with balance N_2 at 902 K and 3.0 atm.

The model is further compared against the IDTs of CH_3CHO measured in an RCM by Tao et al. [48], covering the temperature range of 734 – 1086 K, pressure of 10 bar, and an equivalence ratio of 1.0. As shown in Fig. 14, the updated model underpredicts the autoignition reactivity of CH_3CHO, while the original model overpredicts the autoignition reactivity. Both models exhibit large disagreement with the experiments, particularly at the high-temperature end. The results of the original model and the updated model show significant difference at low temperatures, which decreases with increasing temperature. Besides, the negative temperature coefficient (NTC) behavior is weakened in the updated model and appears at a lower temperature range.

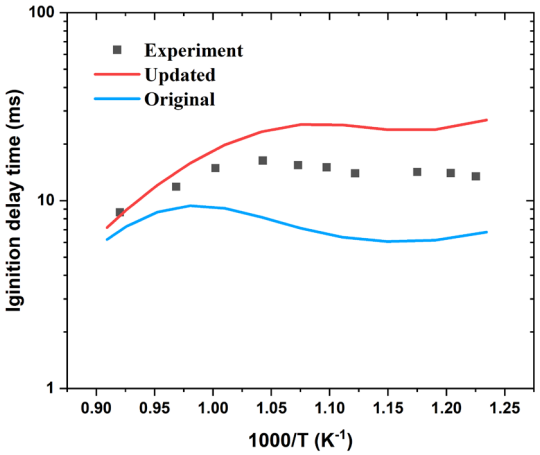

Fig. 14. IDT of CH_3CHO/O_2/Ar mixture at 734–1086 K and 10 bar. Symbols: experimental results [48]; Blue line: simulation results by original model; Red line:

simulation results by updated model.

Figure 15 shows the comparison between experimental results and simulation results of mole fraction of CH_3CHO and CH_3OO at an equivalence ratio of 0.5. The experiments are taken from Zhang et al. [21], who investigated the CH_3CHO oxidation in a JSR at temperatures from 460 to 900 K, equivalence ratios from 0.5 to 4.0, and pressures of 710–720 Torr. It is found that the oxidation onset temperatures predicted by updated and original models are higher than experimental results. Both models underpredict CH_3CHO oxidation at lower temperatures while overpredicting at higher temperatures. However, the updated model shows lower reactivity than the original model before 820 K and becomes more active after 820 K.

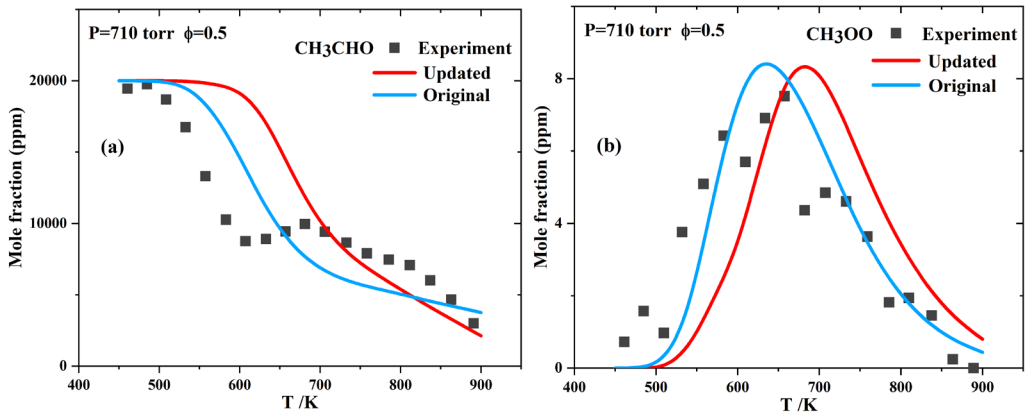

Fig. 15. Mole fraction profiles of (a) CH_3CHO and (b) CH_3OO at equivalence ratio of 0.5 and 710 torr in a JSR. Symbols: experimental results [21]; Blue line: simulation results by original model; Red line: simulation results by updated model.

Fieweger et al. [49,50] measured the IDT of CH_3OH without dilution in a high-pressure shock tube at the temperature range of 800 to 1200 K, equivalence ratio of 1, and pressures of 13 bar and 40 bar. As indicated in Fig. 16, similar to CH_2O, these recalculated reactions almost have no impact on the model performance in predicting the IDT of CH_3OH. Nevertheless, simulation results by both models are in good agreement with experimental results at 13 bar and 40 bar.

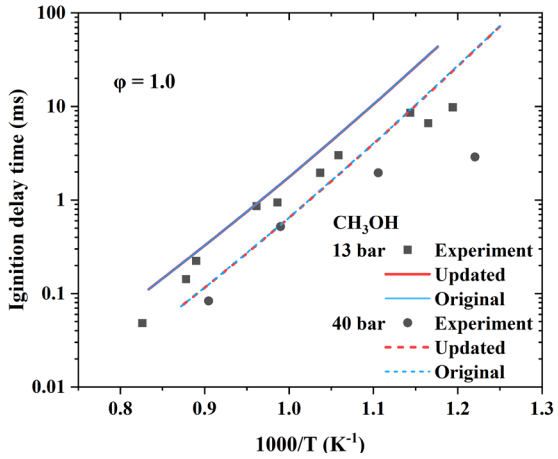

Fig. 16. The IDT of CH_3OH at equivalence ratio of 1 and pressures of 13 bar and 40 bar. Symbols: experimental results [49,50]; Blue line: simulation results by original model; Red line: simulation results by updated model.

Figure 17 shows the autoignition characteristics of C_2H_5OH reported by Cheng et al. [44], which were conducted in a twin-piston rapid compression machine at pressures of 20 and 40 bar, intermediate temperatures from 750 to 980 K, and two fuel loading conditions. It is found that the updated model is less reactive than the original model, predicting longer IDTs for C_2H_5OH, which is more obvious in the lower temperature range. The temperature dependence of autoignition characteristics of C_2H_5OH is accurately captured by the updated model.

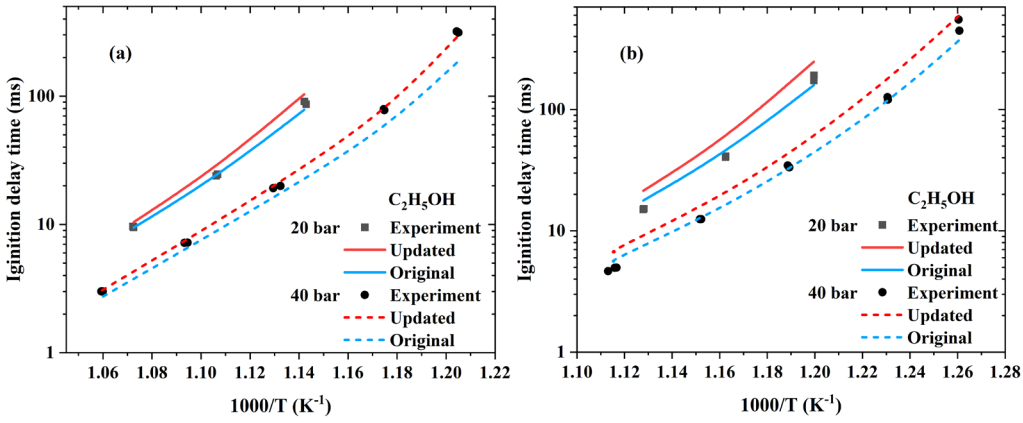

Fig. 17. The IDT of C_2H_5OH conducted at pressures of 20 and 40 bar and temperature range of 750 – 980 K. Symbols: experimental results [44]; Blue lines: simulation results by original model; Red lines: simulation results by updated model. (a) C_2H_5OH: 3.7%, O_2: 11.1%, N_2: 42.5%, Ar: 42.7%; (b) C_2H_5OH: 6.5%, O_2: 19.6%, N_2: 22.1%, Ar: 51.8%.

The original and updated models are also compared against the IDTs of C_2H_5OH/

/O_2/N_2/Ar mixtures measured by Mittal et al. [51], covering a range of pressures (10 – 50 bar), temperatures (825 – 985 K), and equivalence ratios (0.3 – 1.0) in an RCM. These experimental results and simulation results are summarized in Fig 18. The IDTs predicted by updated model are longer than that by original model and are in better agreement with experimental results, especially at lower temperatures. It is worth noting that volume history profiles are not accessible in [51]. Therefore, heat loss effect from the adiabatic core is not considered in the simulation. Nevertheless, heat loss effects will extend the simulated IDTs and are stronger at lower temperatures due to the longer ignition delay times. As such, the slopes of the IDT lines will become steeper with heat loss being considered, resulting in a better agreement in temperature dependence with the experimental results.

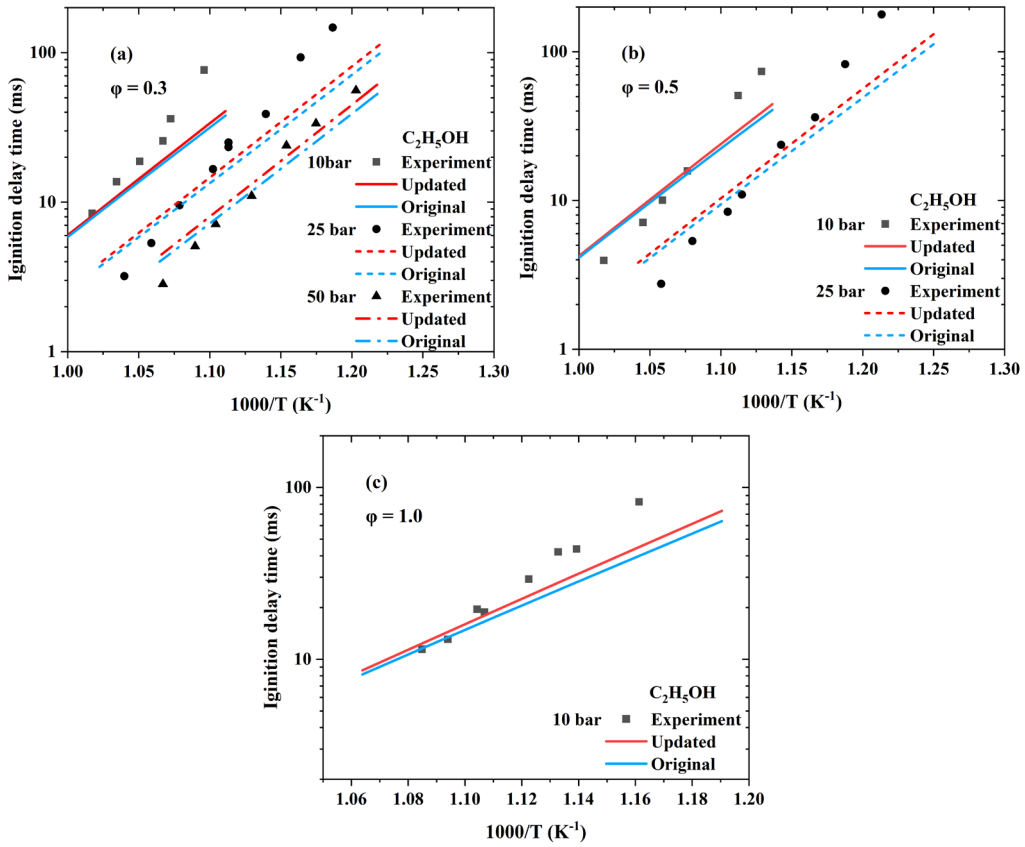

Fig. 18. The IDT of C_2H_5OH measured in an RCM at temperatures of 825 – 985 K. Symbols: experimental results [51]; Blue lines: simulation results by original model; Red lines: simulation results by updated model. (a) φ = 0.3; (b) φ = 0.5; (c) φ = 1.0.

The updated and original models are also validated against the IDTs of NC_3H_7OH from Cheng et al. [39] and Pelucchi et al. [52]. Data from Cheng et al. [44] are measured at the same condition as C_2H_5OH mentioned above, while Pelucchi et al. [52] conducted the IDT experiments in an RCM at temperatures of 704 – 935 K, pressures of 10 and

30 bar, and an equivalence ratio of 1. These validating results are shown in Fig. 19 (a) and (b), respectively. As can be seen in Fig. 19, the model reactivity is lowered uniformly at all temperatures after the rate coefficients of calculated reactions are updated. The IDTs are predicted accurately by both models. The updated model shows a better performance in matching the experimental results from Cheng et al. [44].

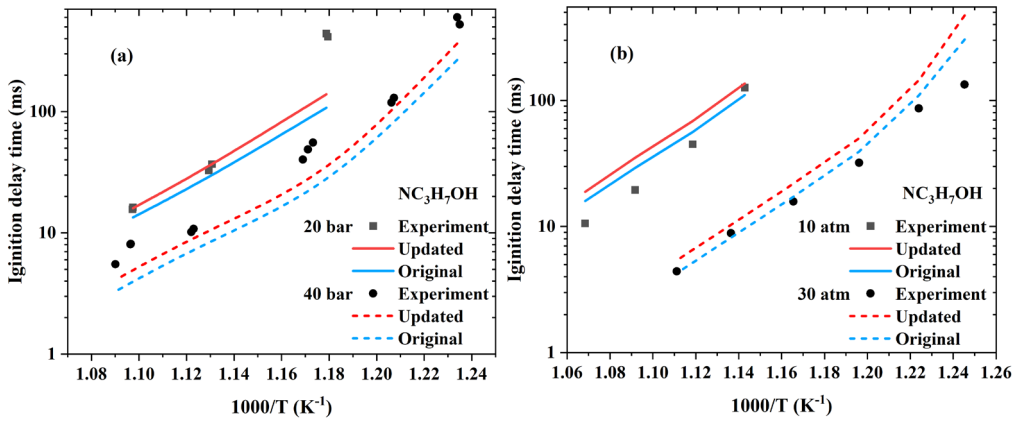

Fig. 19. The IDTs of NC_3H_7OH. Symbols: experimental results; Blue lines: simulation results by original model; Red lines: simulation results by updated model. (a) Data from [44]. (b) Data from [52].

The IDTs of IC_3H_7OH measured by Cheng et al. [44] at the same condition as C_2H_5OH are adopted herein for comparison between the updated and original models in predicting the combustion characteristics of IC_3H_7OH. It is clear in Fig. 20 that the updated model only shows slight differences from the original model, with reduced model reactivity for IC_3H_7OH at all conditions. Both models capture well with the experimental results at different temperatures and pressures.

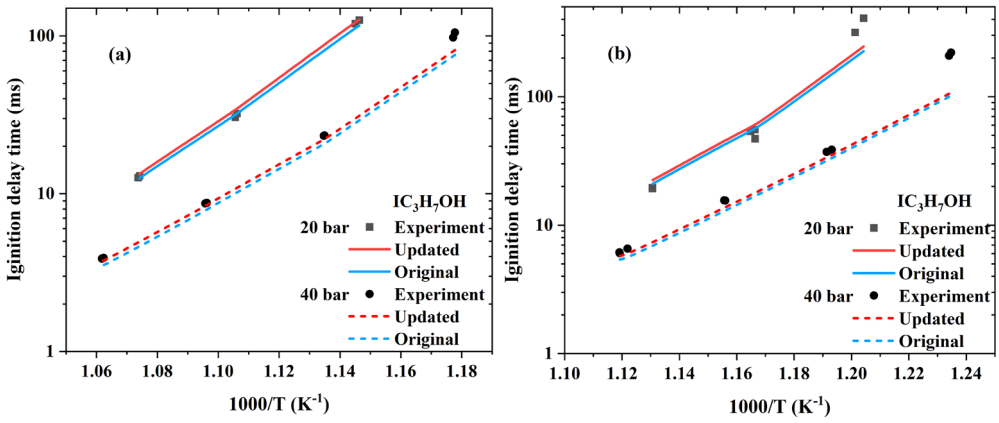

Fig. 20. The IDTs of IC_3H_7OH at temperatures of 750 – 980 K. Symbols: experimental results [44]; Blue lines: simulation results by original model; Red lines: simulation results by updated model. (a) IC_3H_7OH: 4.4 %, O_2: 20 %, N_2: 22.6 %, Ar:

53 %; (b) IC_3H_7OH: 2.5 %, O_2: 11.3 %, N_2: 43 %, Ar: 43.2 %.

3.5 Sensitivity analysis

To investigate the kinetics leading to the difference between the original model and the updated model, brute force sensitivity analysis on the IDT is conducted for CH_2O, CH_3CHO, CH_3OH, C_2H_5OH, NC_3H_7OH, and IC_3H_7OH. The sensitivity coefficients are defined as $S_{rel} = \ln(\frac{\tau^{\Delta}}{\tau})/\ln(\frac{k^{\Delta}}{k})$, where τ^{Δ} is the main IDT after multiplying the original rate constant by 2, i.e., $k^{\Delta} = 2 * k$, and τ is the original ignition delay time. Negative sensitivity coefficients indicate that the reaction promotes reactivity, while positive coefficients indicate an inhibiting effect. Figure 21 presents the computed sensitivity coefficients for the 15 most sensitive reactions of each fuel. Only sensitivity coefficients at 780 K, 20 bar, and equivalence ratio of 1.0 are presented in the paper, while results at other temperatures and pressures are included in the Supplementary Material.

As shown in Fig. 21 (a), though the 15 most sensitive reactions are listed, only 4 reactions show a dominating effect on the CH_2O. The sensitivity coefficients computed by the original model are almost the same as by the updated model, indicating that calculated reactions by this study have a minor impact on the oxidation mechanism of CH_2O. This trend corroborates the results shown in Fig. 13. On the other hand, as shown in Fig. 21 (b), the aldehydic hydrogen abstraction by $CH_3O\dot{O}$ is the most sensitive reaction for CH_3CHO, i.e., $CH_3CHO+CH_3O\dot{O} = CH_3CO+CH_3O_2H$, whose promotion effect is weakened significantly in the updated model. In addition, the inhibiting effect from the top inhibiting reaction, i.e., $HO_2+HO_2 = H_2O_2+O_2$, is enhanced in the updated model. These changes lead to the lower reactivity of the updated model in predicting the CH_3CHO oxidation and autoignition, as shown in Fig. 14 and 15.

Similar to CH_2O, the sensitivity coefficients of CH_3OH (Fig. 21 (c)) computed by original model are nearly identical to the values computed by the updated model, which again aligns well with the results shown in Fig. 16. For C_2H_5OH (Fig. 21 (d)), the top promoting reaction is H-atom abstraction by HO_2 from secondary site of C_2H_5OH, which only changes slightly after updating the calculated reactions. While the third promoting reaction $CH_3CHO+HO_2 = CH_3CO+H_2O_2$ shows the greatest decrease after updating the rate coefficients, indicating its weakened promoting effect. The sensitivity coefficients of H-atom abstraction by CH_3OO radical reactions, i.e., $C_2H_5OH+CH_3O\dot{O} = C_2H_4OH\_S+CH_3O_2H$ and $CH_3CHO+CH_3O\dot{O} = CH_3CO+CH_3O_2H$, also decrease significantly in the updated model, showing their smaller promoting impact. These changes result in the longer IDTs predicted by the updated model for C_2H_5OH (c.f. Fig. 17 and 18). As shown in Fig. 21 (e), when compared with original model, the sensitivity

coefficient of the top promoting reaction $NC_3H_7OH+OH = NC_3H_6OH\_P+H_2O$ shows an obvious decrease in the updated model, leading to the lower reactivity of updated model (c.f. Fig. 19). The sensitivity coefficients of IC_3H_7OH computed by the updated model are quite similar to those by the original model, as indicated by Fig. 21 (f). Therefore, the predicted IDTs of IC_3H_7OH only differ slightly, as illustrated in Fig. 20. It is also seen from Fig. 21 (f) that the H-atom abstraction by $CH_3O\dot{O}$ from the secondary and tertiary sites of IC_3H_7OH shows somewhat promoting effects on the autoignition reactivity of IC_3H_7OH.

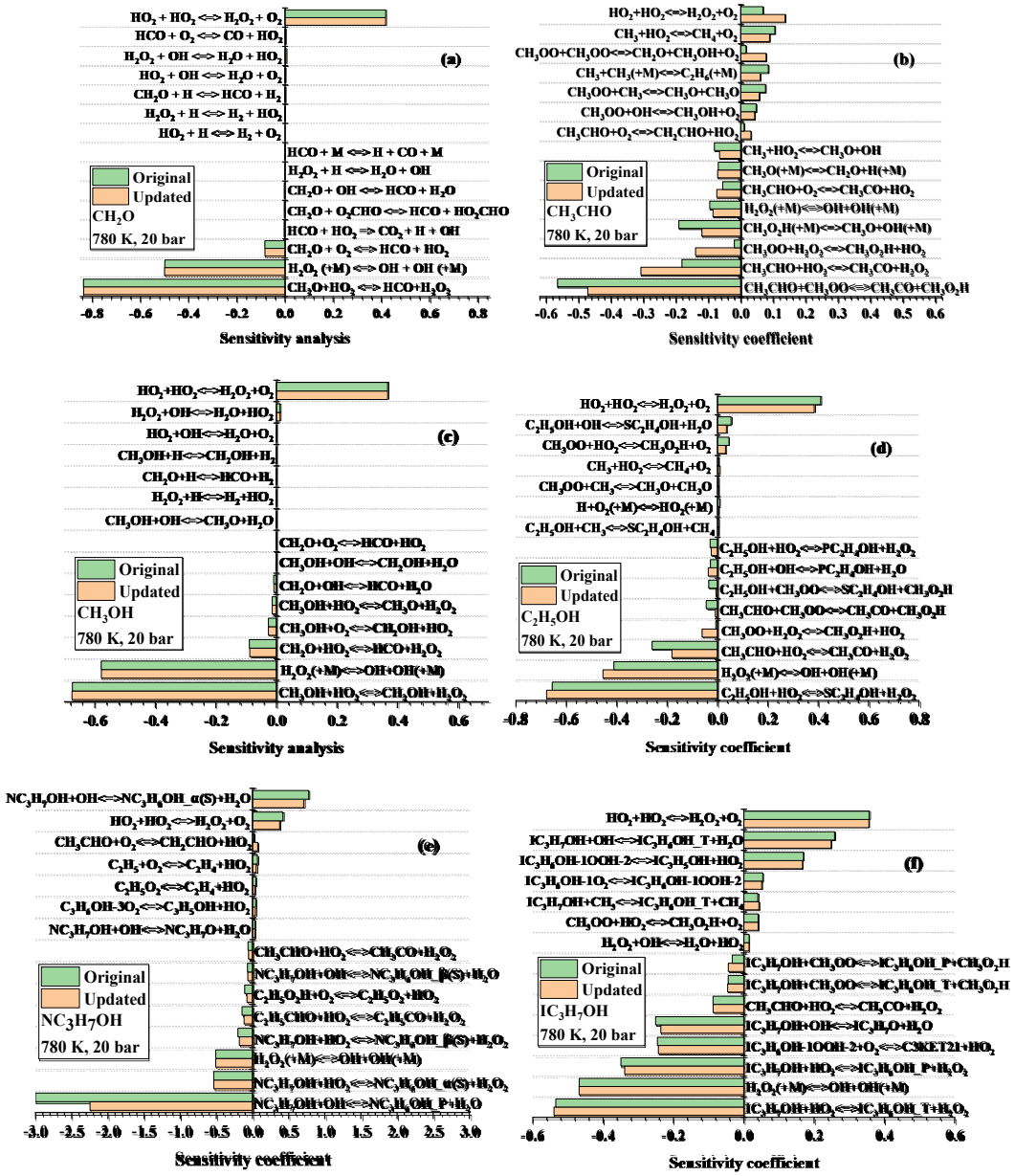

Fig. 21. Sensitivity analysis on ignition delay time for the updated original and updated models at 780 K and 20 bar. (a) CH_2O, (b) CH_3CHO, (c) CH_3OH, (d) C_2H_5OH, (e) NC_3H_7OH, (f) IC_3H_7OH.

3.6 Flux analysis

Flux analyses are further conducted at T=780 K, P=20 bar, equivalence ratio of 1.0, and 5% fuel consumption for CH_2O, CH_3CHO, CH_3OH, C_2H_5OH, NC_3H_7OH, and IC_3H_7OH, which are summarized in Fig. 22-27. The percentages shown in Fig. 22-27 are computed as the ratio of the rate of consumption for that pathway to the total rate of consumption.

Figure 22 shows the flux analysis results of CH_2O. At 5% CH_2O consumption, H-atom of CH_2O is mainly abstracted by HO_2 leading to the formation of HCO, which then mainly reacts with O_2 to form CO that further produces CO_2. Due to the lack of CH_3 radical to form $CH_3O\dot{O}$ via O_2 addition, the primary reaction pathway of CH_2O does not involve $CH_3O\dot{O}$ radical. This explains the negligible impact of the updated rate parameters on the model performance in predicting the oxidation of CH_2O (c.f. Fig. 13). As a result, the branching ratios computed by original model and updated models are very similar. It should be noted that this does not mean that H-atom abstraction by $CH_3O\dot{O}$ from CH_2O is not important, which will be discussed in the following.

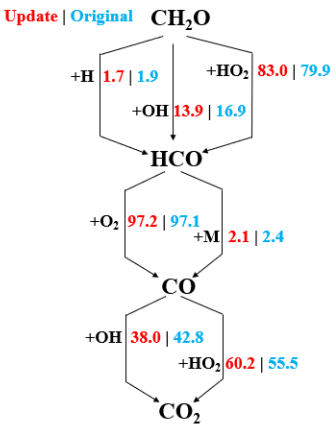

Fig. 22. The flux analysis results of CH_2O at 780 K, 20 bar, and equivalence ratio of 1.0, and 5% fuel consumption. Red numbers: branching ratio computed by updated model; blue numbers: branching ratio computed by original model.

Figure 23 summarizes the flux analysis results of CH_3CHO. The dehydrogenation of CH_3CHO usually occurs on the aldehydic hydrogen site, forming a CH_3CO radical. CH_3CO subsequently decomposes to produce a CH_3 radical, which then reacts with O_2 to generate a $CH_3O\dot{O}$ radical. During the low temperature oxidation of CH_3CHO, this pathway dominates, as shown in Fig. 23, leading to the abundant formation of $CH_3O\dot{O}$ radicals. The produced $CH_3O\dot{O}$ radicals become significant, and largely participate in the H-atom abstractions of CH_3CHO and CH_2O. Due to the importance of these

pathways, updating their rate coefficients leads to significant changes in the low temperature oxidation pathways. As can be seen from Fig. 23, with the implementation of the updated rates, the branching ratio of H-atom abstraction by $CH_3O\dot{O}$ from CH_3CHO decreasing from 31.7% to 6.5, while the H-atom abstraction by HO_2 from CH_3CHO is enhanced, i.e., from 8.9% to 23.8%. These trends agree well with the sensitivity analysis results shown in Fig. 21 (b) where the promotion effect of $CH_3CHO+CH_3O\dot{O}$ = $CH_3CO+CH_3O_2H$ decreases and that of $CH_3CHO+HO_2$ = $CH_3CO+H_2O_2$ increases. In addition, there is an obvious shift toward $CH_3O\dot{O}+H_2O_2$ = $CH_3O_2H+HO_2$, where the produced HO_2 can further participate in H-atom abstractions from CH_3CHO. Correspondingly, there is a distinct growth in the sensitivity coefficient of this promoting reaction, as shown in Fig. 21 (b).

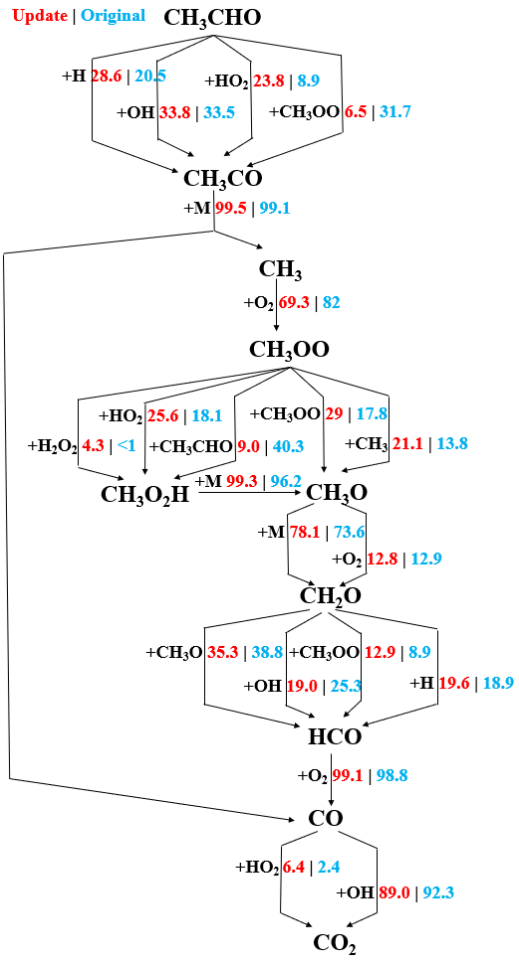

Fig. 23. The flux analysis results of CH_3CHO at 780 K, 20 bar, and equivalence ratio of 1.0, and 5% fuel consumption. Red numbers: branching ratio computed by updated model; blue numbers: branching ratio computed by original model.

Figure 24 shows the flux analysis results of CH_3OH. The H-atom of CH_3OH is

abstracted by OH and HO_2 radicals. The produced CH_2OH mainly reacts with O_2 to form CH_2O. Thereafter, CH_2O oxidation follows the same pathway as shown in Fig. 22, which eventually leads to the formation of CO_2. Similar to that observed for CH_2O, $CH_3O\dot{O}$ radical is absent from the primary oxidation pathway of CH_3OH, due largely to lack of CH_3 production. As such, very similar branching ratios are observed between the updated model and the original model. Therefore, the updated model shows no difference in predicting the combustion characteristic of CH_3OH from the original model, as observed in Fig. 16.

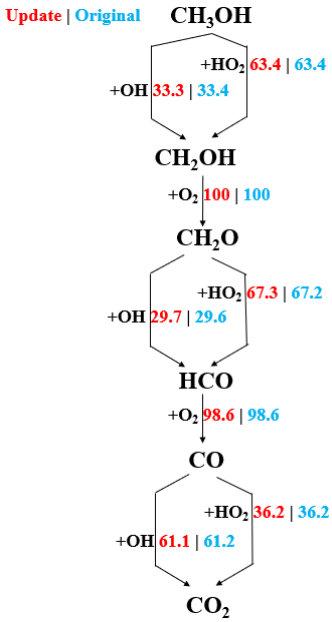

Fig. 24. The flux analysis results of CH_3OH at 780 K, 20 bar, and equivalence ratio of 1.0, and 5% fuel consumption. Red numbers: branching ratio computed by updated model; blue numbers: branching ratio computed by original model.

Figure 25 shows the flux analysis results of C_2H_5OH. The H-atom at the secondary site of C_2H_5OH is easier to be abstracted compared to the primary H site. After removing two H-atoms from C_2H_5OH (one from the secondary site and another from the OH group), CH_3CHO is formed. Then CH_3CHO is consumed following the same reaction pathways as in Fig. 23, where $CH_3O\dot{O}$ radicals are considerably produced. The produced $CH_3O\dot{O}$ radical further abstracts H-atom from CH_2O, CH_3CHO and C_2H_5OH, and competes with other radicals such as OH and HO_2. Compared to the original model, the contribution of H-atom abstraction by $CH_3O\dot{O}$ radicals is weakened in the updated model, with the branching ratio of $CH_3O\dot{O}$ abstracting H-atom decreasing from 11.3% to 1.3% for CH_3CHO, and 4.4% to less than 1.0% for C_2H_5OH. These support the sensitivity analysis results shown in Fig. 21 (d), with sensitivity coefficients of

$CH_3CHO+CH_3O\dot{O} = CH_3CO+CH_3O_2H$ and $C_2H_5OH+CH_3O\dot{O} = C_2H_4OH\_S+CH_3O_2H$ decreasing significantly in updated model. When comparing the oxidation pathway of C_2H_5OH with CH_3CHO, it is found that $CH_3O\dot{O}$ radical has less contribution in C_2H_5OH consumption, with only 4.4% of C_2H_5OH consumed by $CH_3O\dot{O}$ radical in C_2H_5OH oxidation (Fig. 25), while as high as 31.7% of CH_3CHO consumed by $CH_3O\dot{O}$ radical in CH_3CHO oxidation (Fig. 23). This is due to $CH_3O\dot{O}$ radical is formed at a relatively later stage of the oxidation process for C_2H_5OH.

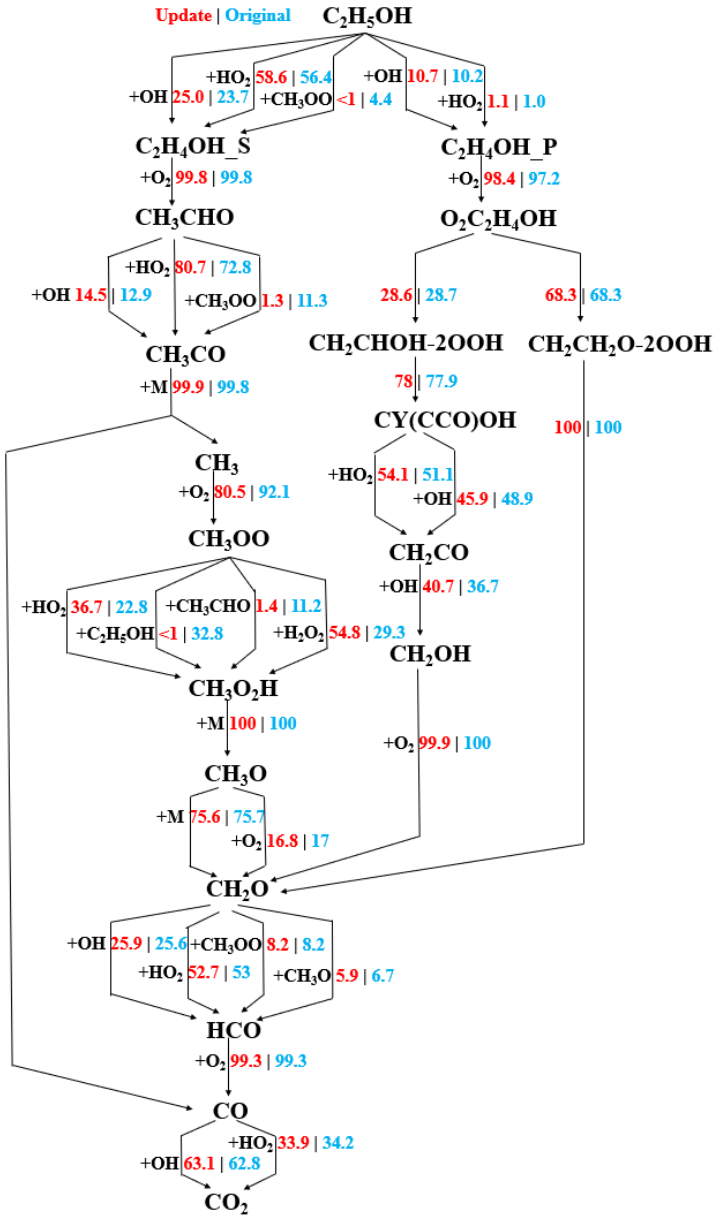

Fig. 25. The flux analysis results of C_2H_5OH at 780 K, 20 bar, and equivalence ratio of 1.0, and 5% fuel consumption. Red numbers: branching ratio computed by updated model; blue numbers: branching ratio computed by original model.

Figure 26 shows the flux analysis results of NC_3H_7OH. The H-atom at the α site is easiest to be abstracted. Similar to the oxidation of C_2H_5OH, the $CH_3O\dot{O}$ radical forms in a relatively later stage, leading to its low participation in H-atom abstraction from CH_3CHO and NC_3H_7OH (i.e., <1% for both, as shown in Fig. 26). Nevertheless, the participation of $CH_3O\dot{O}$ still significantly impacts the reactivity of model for NC_3H_7OH, as can be seen from Fig. 19. The most obvious difference between updated model and original model is that $CH_3O\dot{O}$ hardly participates in the H-atom abstraction from NC_3H_7OH and CH_3CHO in the updated model, while 42.6% of $CH_3O\dot{O}$ participates in the H-atom abstraction from NC_3H_7OH in the original model. Similar to CH_3CHO and C_2H_5OH, more $CH_3O\dot{O}$ reacts with H_2O_2 in the updated model than the original model, forming HO_2. This shift in $CH_3O\dot{O}$ consumption reduces the model reactivity, as the H_2O_2 could have been decompose to produce two OH radicals.

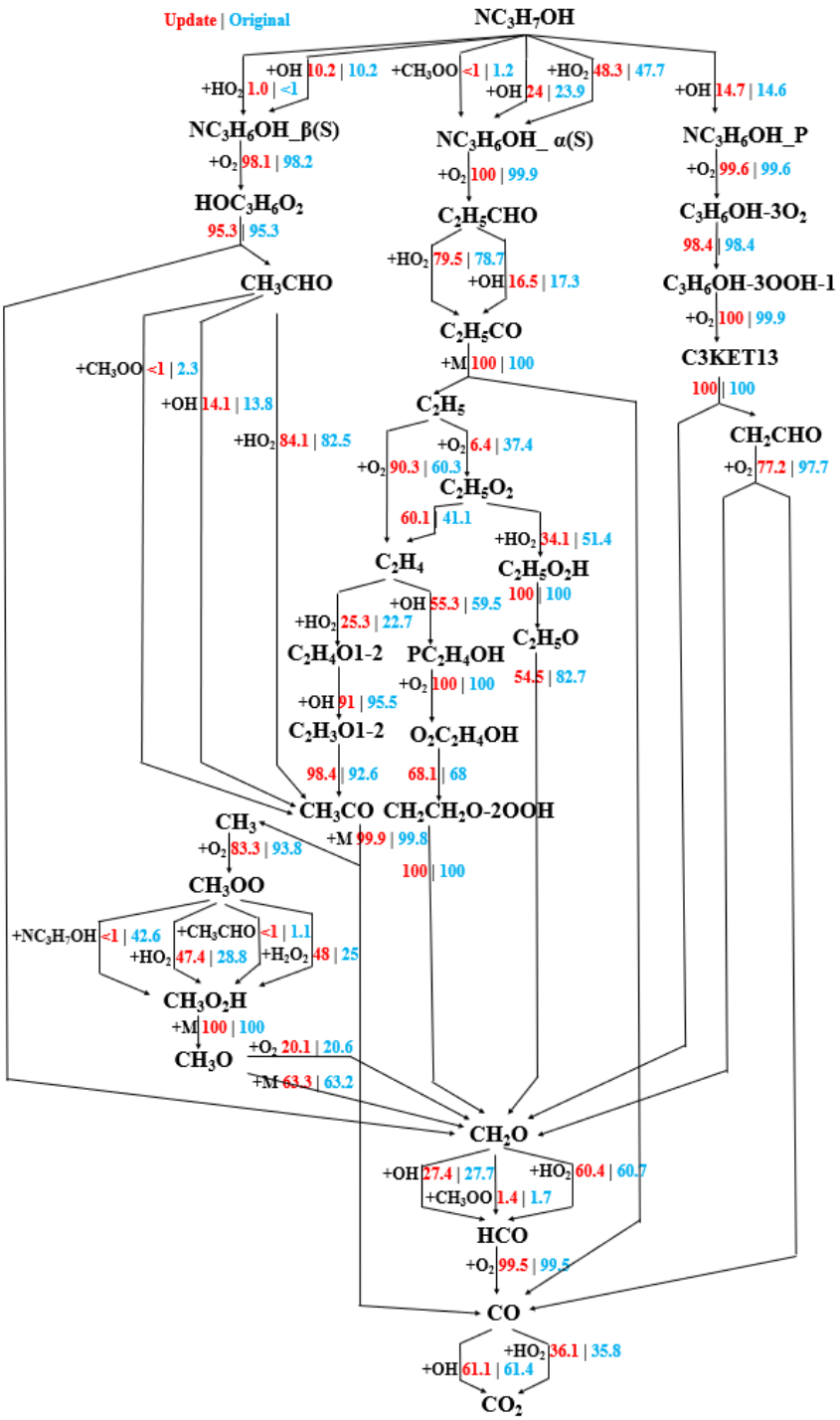

Fig. 26. The flux analysis results of NC_3H_7OH at 780 K, 20 bar, and equivalence ratio of 1.0, and 5% fuel consumption. Red numbers: branching ratio computed by updated model; blue numbers: branching ratio computed by original model.

Figure 27 shows the flux analysis results of IC_3H_7OH. It can be seen that H-atom abstraction favors the secondary site of IC_3H_7OH, leading to the formation of $IC_3H_6OH\_S$. The branching ratios shown in Fig. 27 are only slightly altered after updating the rate parameters of the calculated reactions. This is due to the $CH_3O\dot{O}$

radical are not significantly formed until the decomposition of CH_3COCH_2O. Prior to this point, abstraction by $CH_3O\dot{O}$ is not important. Nevertheless, $CH_3O\dot{O}$ later abstracts H-atom from CH_2O and CH_3CHO. These pathways are slightly weakened in the updated model, as shown in Fig. 27, hence a slightly reduced model reactivity.

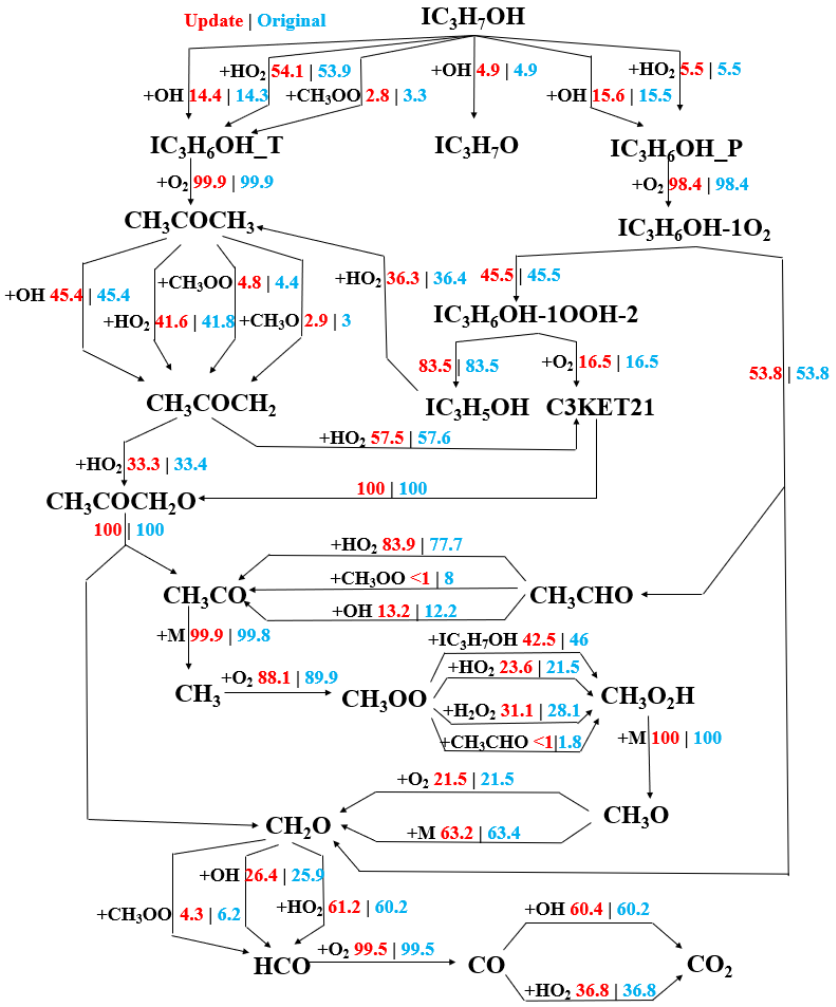

Fig. 27. The flux analysis results of IC_3H_7OH at 780 K, 20 bar, and equivalence ratio of 1.0, and 5% fuel consumption. Red numbers: branching ratio computed by updated model; blue numbers: branching ratio computed by original model.

4. Implications for model development

It is obvious from the flux analysis results shown in Fig. 22-27 that CH_2O and CH_3CHO chemistry are extremely important, as they mark the final steps of oxidation of all the investigated hydrocarbons with carbon number >1. Small perturbations to the chemistry of these two can lead to significant changes in the model performance. This is confirmed in Fig. 14, 15, 17, 18, 19 and 20, where modifications on the rate parameters for only one type of reaction, i.e., H-atom abstraction by $CH_3O\dot{O}$, change the model performance considerably. More investigations are needed in the future to

adequately address the chemistry of these two compounds, via theoretical calculations (e.g., this study), model optimization [53], refitting (e.g., a forthcoming study from the author's group), and fundamental experiments. However, this has been insufficiently addressed in the past. For instance, most previous fundamental experiments for CH_2O [54][55] have been conducted at high temperatures, while those at low to intermediate temperatures and high pressures are seriously lacking. Additionally, existing studies on fundamental combustion of CH_3CHO have been focusing on pressure conditions below 10 bar, and autoignition experiments at higher pressure and lower temperatures (e.g., < 900 K) have been missing (to the authors knowledge, there is only one study on CH_3CHO autoignition within the low-temperature regime [48]). Due to the lack of fundamental experiments, the chemistry models today for large hydrocarbons are ill-conditioned on an insufficiently described core chemistry model for CH_2O and CH_3CHO. This paper serves as an obvious indication of such insufficiency. Specifically, the model adopted by this study show a good performance in predicting the IDTs of ethanol (as shown in Fig. 17-18) and propanols (as shown in Fig. 19-20), while showing large inadequacies in predicting the oxidation profiles of CH_2O (shown in Fig. 13), IDTs of CH_3CHO (shown in Fig. 14), and oxidation profiles of CH_3CHO (shown in Fig. 15). This indicates that the physical representation of the base oxidation chemistry in the model, particularly those for CH_2O and CH_3CHO, is not adequate and needs to be reevaluated.

Conclusion

This work presents a systematic study of H-atom abstraction by $CH_3O\dot{O}$ from different sites of CH_2O, CH_3CHO, CH_3OH, C_2H_5OH, NC_3H_7OH, and IC_3H_7OH. The geometry optimizations and vibrational frequencies of all the involved species were conducted at M06-2X/6-311++G(d,p) level of theory. The SPEs were determined using QCISD(T)/cc-pVXZ (where X = D and T) and MP2/cc-pVXZ (where X = D, T, and Q). The energy barriers of the investigated 11 reactions are obtained. The temperature dependent rate coefficients of these 11 reactions are proposed at the temperature range of 298.15-2000 K, based on conventional transition state theory with unsymmetric Eckart tunneling corrections. Updated rate constants for these reactions are further incorporated into a recently updated chemistry model, where their influences on model performance are investigated via comprehensive kinetic modeling. Sensitivity and flux analyses are further conducted to explore the chemical kinetics governing changes in model performances. The primary conclusions from this study are:

- The energy barrier for H-atom abstraction from the ν site of CH_3CHO is the lowest, while it is highest for H-atom abstraction from the primary site of C_2H_5OH. For alcohols, at low temperatures, the rate coefficients for H-atom

abstraction from the α site are the largest, followed by the β site, and finally followed by the γ site. For CH_2O and CH_3CHO, the rate coefficients for the abstraction of aldehydic hydrocarbon are quite similar. At intermediate to high temperatures, the discrepancy between H-atom abstraction from primary sites of the involved species is relatively small, except for C_2H_5OH, which is considerably lower. For H-atom abstraction from the α site, IC_3H_7OH has the highest rate coefficient.

- After updating the rate parameters of calculated reactions, the kinetic model becomes less reactive in predicting the oxidation and autoignition of CH_3CHO, C_2H_5OH, NC_3H_7OH and IC_3H_7OH, while exhibiting negligible change in model prediction for CH_2O and CH_3OH. Additionally, the updated model captures reasonably well the fundamental experiments for alcohols, while showing large discrepancies for aldehydes.
- Sensitivity and flux analyses reveal the kinetics governing the diverse changes in model performance and the characteristically different oxidation pathways between the C_1 species (i.e., CH_2O and CH_3OH) and their heavier counterparts. Specifically,
  - with the updated rate parameters, there is an obvious decrease in the contribution of H-atom abstractions by $CH_3O\dot{O}$ from fuel molecules and their derivatives, which is responsible for the reduced model reactivity for CH_3CHO, C_2H_5OH, NC_3H_7OH and IC_3H_7OH.
  - The minor impact of the updated rate parameters on model performance for CH_2O and CH_3OH can be attributed to their lack of ability to produce CH_3 radicals.
- Further analyses highlight the critical roles of CH_2O and CH_3CHO sub-chemistries, which have been ill-conditioned in existing models, in developing adequate chemistry models for large hydrocarbons, and call for future efforts to improve the current CH_2O and CH_3CHO chemistries.

Acknowledgement

The work is supported by the Research Grants Council of the Hong Kong Special Administrative Region, China under PolyU P0034937 and PolyU P0039589, as well as by the Natural Science Foundation of Guangdong Province under 2023A1515010976.

Reference

[1] Z. Yang, C. Fei, Y. Li, D. Wang, C. Sun, Experimental study of the effect of physical and chemical properties of alcohols on the spray combustion characteristics of alcohol-

diesel blended fuels, Energy 263 (2023) 126158.
[2] M. N. Nabi, H. Ogawa, N. Miyamoto, Nature of Fundamental Parameters Related to Engine Combustion for a Wide Range of Oxygenated Fuels, SAE Tech. 2002-01-2853, 2002.
[3] M. russtar, M. tuhldreher, D. wain, W. idgeon, High Efficiency and Low Emissions from a Port-Injected Engine with Neat Alcohol Fuels. SAE Tech. 2002-01-2743, 2002.
[4] Y. Shekar Kuppili, P. Kumar, S. Singh Sandhu, A critical review of the impacts of split injection strategies on the performance, combustion and emissions characteristics of a diesel engine fueled with low carbon alcohol fuels, Mater. Today: Proc. 72 (2023) 2928-2932.
[5] A. Jamrozik, The effect of the alcohol content in the fuel mixture on the performance and emissions of a direct injection diesel engine fueled with diesel-methanol and diesel-ethanol blends, Energy Convers. Manage.148 (2017) 461-476.
[6] C. Sayin, Engine performance and exhaust gas emissions of methanol and ethanol–diesel blends, Fuel 89 (2010) 3410-3415.
[7] R. Chen, K. Nishida, B. Shi, Characteristics of combustion and soot formation of ethanol-gasoline blends injected by a hole-type nozzle for direct-injection spark-ignition engines, Fuel Process. Technol. 181 (2018) 318-330.
[8] S. Cheng, S. Scott Goldsborough, C. Saggese, S.W. Wagnon, W.J. Pitz, New insights into fuel blending effects: Intermolecular chemical kinetic interactions affecting autoignition times and intermediate-temperature heat release, Combust. Flame 233 (2021) 111559.
[9] S. Cheng, D. Kang, A. Fridlyand, S.S. Goldsborough, C. Saggese, S. Wagnon, M.J. McNenly, M. Mehl, W.J. Pitz, D. Vuilleumier, Autoignition behavior of gasoline/ethanol blends at engine-relevant conditions, Combust. Flame 216 (2020) 369-384.
[10] M. Pelucchi, K.P. Somers, K. Yasunaga, U. Burke, A. Frassoldati, E. Ranzi, H.J. Curran, T. Faravelli, An experimental and kinetic modeling study of the pyrolysis and oxidation of n-C3C5 aldehydes in shock tubes, Combust. Flame 162 (2015) 265-286.
[11] P. Dagaut, M. Reuillon, D. Voisin, M. Cathonnet, M. McGuinness, J.M. Simmie, Acetaldehyde Oxidation in a JSR and Ignition in Shock Waves: Experimental and Comprehensive Kinetic Modeling, Combust. Sci. Technol. 107 (1995) 301-316.
[12] K.P. Shrestha, L. Seidel, T. Zeuch, F. Mauss, Kinetic Modeling of NOx Formation and Consumption during Methanol and Ethanol Oxidation, Combust. Sci. Technol. 191 (2019) 1627-1659.
[13] K. Kohse-Hoinghaus, P. Osswald, T.A. Cool, T. Kasper, N. Hansen, F. Qi, C.K. Westbrook, P.R. Westmoreland, Biofuel combustion chemistry: from ethanol to biodiesel, Angew. Chem. Int. Ed. Engl 49 (2010) 3572-3597.

[14] S. Cheng, C. Saggese, D. Kang, S.S. Goldsborough, S.W. Wagnon, G. Kukkadapu, K. Zhang, M. Mehl, W.J. Pitz, Autoignition and preliminary heat release of gasoline surrogates and their blends with ethanol at engine-relevant conditions: Experiments and comprehensive kinetic modeling, Combust. Flame 228 (2021) 57-77.
[15] H. J. Curran, P. Gaffuri, W. J. Pitz, C. K. Westbrook, A Comprehensive Modeling Study of n-Heptane Oxidation, Combust. Flame 114 (1998) 149-177.
[16] H.J. Curran, Developing detailed chemical kinetic mechanisms for fuel combustion, Proc. Combust. Inst. 37 (2019) 57-81.
[17] S. Kuzhanthaivelan, B. Rajakumar, Theoretical investigations on the kinetics of dimethoxymethane with peroxy radicals, Chem. Phys. Lett. 756 (2020) 137846.
[18] H. H. Carstensen, A.M. Dean, O. Deutschmann, Rate constants for the H abstraction from alkanes (R–H) by R′O2 radicals: A systematic study on the impact of R and R′, Proc. Combust. Inst. 31 (2007) 149-157.
[19] H.T. Guo, Y. Tang, S.H. Liu, Y. Ma, S. Fang, H.J. Curran, C.W. Zhou, Kinetic Properties Study of H Atom Abstraction by CH3O2 Radicals from Fuel Molecules with Different Functional Groups, J. Phys. Chem. A. 127 (2023) 1960-1974.
[20] G. Shi, J. Song, B. Su, M. Chen, Mechanistic study of the reaction of methyl peroxy radical (CH3O2) with formaldehyde (CH2O), Mol. Phys. 117 (2018) 298-302.
[21] X. Zhang, L. Ye, Y. Li, Y. Zhang, C. Cao, J. Yang, Z. Zhou, Z. Huang, F. Qi, Acetaldehyde oxidation at low and intermediate temperatures: An experimental and kinetic modeling investigation, Combust. Flame 191 (2018) 431-441.
[22] Z. Zhao, J. Song, B. Su, X. Wang, Z. Li, Mechanistic Study of the Reactions of Methyl Peroxy Radical with Methanol or Hydroxyl Methyl Radical, J. Phys. Chem. A. 122 (2018) 5078-5088.
[23] G. Shi, J. Song, F. Cao, G. Lv, Z. Li, Mechanistic studies and rate coefficients calculations of hydrogen abstraction from ethanol by methyl peroxy radical and hydroperoxyl radical, Mol. Phys. 118 (2020).
[24] C. Yang, J.-T. Chen, X. Zhu, X. Bai, Y. Li, K.K. Yalamanchi, S.M. Sarathy, S. Scott Goldsborough, S. Cheng, H.J. Curran, C.-W. Zhou, From electronic structure to model application of key reactions for gasoline/alcohol combustion: Hydrogen-atom abstraction by CH3OȮ radicals, Proc. Combust. Inst. 39 (2023) 415-423.
[25] Y. Zhao, D. G. Truhlar, The M06 Suite of Density Functionals for Main Group Thermochemistry, Thermochemical Kinetics, Noncovalent Interactions, Excited States, and Transition Elements: Two New Functionals and Systematic Testing of Four M06-class Functionals and 12 other Functionals. Theor. Chem. Acc. 120 (2008) 215−241.
[26] A. McLean, G. Chandler, Contracted Gaussian Basis Sets for Molecular Calculations. I. Second Row Atoms, Z = 11−18. J. Chem. Phys. 72 (1980) 5639−5648.
[27] W. J. Hehre, R. Ditchfield, J. A. Pople, Self-consistent Molecular Orbital Methods.

XII. Further Extensions of Gaussian-type Basis Sets for Use in Molecular Orbital Studies of Organic Molecules. J. Chem. Phys. 56 (1972) 2257−2261.
[28] J. A. Pople, M. Head - Gordon, K. Raghavachari, Quadratic configuration interaction. A general technique for determining electron correlation energies, J. Chem. Phys. 87 (1987) 5968–5975.
[29] M. Head-Gordon, T. Head-Gordon, Analytic MP2 Frequencies without Fifth-order Storage. Theory and Application to Bifurcated Hydrogen Bonds in the Water Hexamer, Chem. Phys. Lett. 220 (1994) 122−128.
[30] P. Zhang, S.J. Klippenstein, C.K. Law, Ab initio kinetics for the decomposition of hydroxy butyl and butoxy radicals of n-butanol, J. Phys. Chem. A 117 (2013) 1890–1906.
[31] J.R. Barker, Multiple-Well, multiple-path unimolecular reaction systems. I. MultiWell computer program suite, Int. J. Chem. Kinet. 33 (2001) 232-245.
[32] Y. Li, S.J. Klippenstein, C.W. Zhou, H.J. Curran, Theoretical Kinetics Analysis for H Atom Addition to 1,3-Butadiene and Related Reactions on the C(4)H(7) Potential Energy Surface, J. Phys. Chem. A. 121 (2017) 7433-7445.
[33] Y. Georgievskii, J.A. Miller, M.P. Burke, S.J. Klippenstein, Reformulation and solution of the master equation for multiple-well chemical reactions, J. Phys. Chem. A 117 (2013) 12146-12154.
[34] J. A. Miller, S.J. Klippenstein, Master Equation Methods in Gas Phase Chemical Kinetics, J. Phys. Chem. A 110 (2006) 10528-10544.
[35] Y. Georgievskii, S.J. Klippenstein, Strange Kinetics of the C2H6 + CN Reaction Explained, J. Phys. Chem. A 111 (2007) 3802-3811.
[36] C. Eckart, The Penetration of a Potential Barrier by Electrons, Phys. Rev. 35 (1930) 1303-1309.
[37] W. Tsang, R. F. Hampson, Chemical Kinetic Data Base for Combustion Chemistry. Part I. Methane and Related Compounds, J. Phys. Chem. Ref. Data. 15 (1986) 1087-1279.
[38] S. L. Fischer, F. L. Dryer, H. J. Curran, The Reaction Kinetics of Dimethyl Ether. I: High Temperature Pyrolysis and Oxidation in Flow Reactors, Int. J. Chem. Kinet. 32 (2000) 713-740.
[39] W. Tsang, Chemical Kinetic Data Base for Combustion Chemistry. Part 2. Methanol, J. Phys. Chem. Ref. Data. 16 (1987) 471-508.
[40] C. Anastasi, D. U. Hancock, Reaction of methylperoxy radicals with methanol and formaldehyde at 600 K, J. Chem. Soc., Faraday Trans. 1, 80 (1984) 935-939
[41] G. Mittal, S. M. Burke, V. A. Davies, B. Parajuli, W. K. Metcalfe, H. J. Curran, Autoignition of ethanol in a rapid compression machine, Combust. Flame 161 (2014) 1164-1171.

[42] M. Mehl, W. J. Pitz, C. K. Westbrook, H. J. Curran, Kinetic modeling of gasoline surrogate components and mixtures under engine conditions, Proc. Combust. Inst. 33 (2011) 193-200.
[43] M. V. Johnson, S. S. Goldsborough, Z. Serinyel, P. O'Toole, E. Larkin, G. O'Malley, H. J. Curran, A Shock Tube Study of n- and iso-Propanol Ignition, Energy. Fuels. 23 (2009) 5886-5898.
[44] S. Cheng, D. Kang, S.S. Goldsborough, C. Saggese, S.W. Wagnon, W.J. Pitz, Experimental and modeling study of C2–C4 alcohol autoignition at intermediate temperature conditions, Proc. Combust. Inst. 38 (2021) 709-717.
[45] C. Saggese, C.M. Thomas, S.W. Wagnon, G. Kukkadapu, S. Cheng, D. Kang, S.S. Goldsborough, W.J. Pitz, An improved detailed chemical kinetic model for C3-C4 linear and iso-alcohols and their blends with gasoline at engine-relevant conditions, Proc. Combust. Inst. 38 (2021) 415-423.
[46] M.J. McNenly, R.A. Whitesides, D.L. Flowers, Faster solvers for large kinetic mechanisms using adaptive preconditioners, Proc. Combust. Inst. 35 (2015) 581-587.
[47] J. Li, Z. Zhao, A. Kazakov, M. Chaos, F.L. Dryer, J.J. Scire, A comprehensive kinetic mechanism for CO, CH2O, and CH3OH combustion, Int. J. Chem. Kinet. 39 (2007) 109-136.
[48] T. Tao, S. Kang, W. Sun, J. Wang, H. Liao, K. Moshammer, N. Hansen, C.K. Law, B. Yang, A further experimental and modeling study of acetaldehyde combustion kinetics, Combust. Flame 196 (2018) 337-350.
[49] K. Fieweger, R. Blumenthal, G. Adomeit, Shock-tube investigations on the self-ignition of hydrocarbon-air mixtures at high pressures, Symp. (Int.) Combust. 25 (1994) 1579-1585.
[50] K. Fieweger, R. Blumenthal, G. Adomeit, Self-Ignition of S.I. Engine Model Fuels: A Shock Tube Investigation at High Pressure, Combust. Flame 109 (1997) 599-619.
[51] G. Mittal, S.M. Burke, V.A. Davies, B. Parajuli, W.K. Metcalfe, H.J. Curran, Autoignition of ethanol in a rapid compression machine, Combust. Flame 161 (2014) 1164-1171.
[52] M. Pelucchi, S. Namysl, E. Ranzi, A. Rodriguez, C. Rizzo, K.P. Somers, Y. Zhang, O. Herbinet, H.J. Curran, F. Battin-Leclerc, T. Faravelli, Combustion of n-C3-C6 Linear Alcohols: An Experimental and Kinetic Modeling Study. Part II: Speciation Measurements in a Jet-Stirred Reactor, Ignition Delay Time Measurements in a Rapid Compression Machine, Model Validation, and Kinetic Analysis, Energ. Fuel 34 (2020) 14708-14725.
[53] S. Cheng, Y. Yang, M.J. Brear, M. Frenklach, Quantifying uncertainty in kinetic simulation of engine autoignition, Combust. Flame 216 (2020) 174-184.
[54] A. M. Dean, R. L. Johnson, D. C. Steiner, Shock-Tube Studies of Formaldehyde

Oxidation, Combust. Flame 37 (1980) 41-62.
[55] Y. Hidaka, T. Taniguchi, H. Tanaka, T. Kamesawa, K. Inami, H. Kawano, Shock-Tube Study of CH2O Pyrolysis and Oxidation, Combust. Flame 92 (1993) 365-376.